Trapped-Mg^+ Apparatus for Control and Structure Studies

Trapped-Mg^+ Apparatus for Control and Structure Studies

By

Laura A Toppozini, B.Sc.

A Thesis

Submitted to the School of Graduate Studies

in Partial Fulfilment of the Requirements

for the Degree

Masters

McMaster University

MASTERS (2006) McMaster University

(Department of Physics and Astronomy) Hamilton, Ontario

TITLE: Trapped-Mg^+ Apparatus for Control and Structure Studies

AUTHOR: Laura Toppozini, B.Sc.

SUPERVISOR: Dr. Brian E. King

NUMBER OF PAGES: xii, 94

Abstract

Trapped ions can be isolated from external perturbations such as collisions with other atoms or electric and magnetic field inhomogeneities. For this reason, trapped ions can be useful in spectral measurements, quantum information technology and studying quantum behaviour. In this thesis, I discuss a trapped-Mg^+ apparatus for studying the quantum mechanics of atoms. I describe the laser interactions that allow us to coherently excite our atoms. I go on to discuss the actual apparatus for trapping ions and making precise measurements, the hyperfine structure of $^{25}Mg^+$ and a proposed linewidth measurement.

Acknowledgements

I would like to take this opportunity to thank my supervisor, Brian E. King. Your patience, determination and knowledge are greatly admired and appreciated. I hope, during my next few years with the group, that I can continue to learn from your example.

I would also like to thank my labmates Jason Nguyen and JiaJia Zhou. I have learned a lot from you both and you make working in the lab much more fun than it should be. You guys are great friends.

Finally, I would like to thank my parents, John and Barbara and my brothers and sisters: William, Johnny, Kimberly and Lisa. Without your support I would have never been able to start this degree let alone finish it. You all mean the world to me. Thank you.

Dedicated to William, Johnny, Kimberly and Lisa

Table of Contents

List of Figures

Chapter 1

Introduction

Ions can be confined by electric fields to a small region in space. This is accomplished by oscillating electric fields whose strength increases away from trap center (i.e. there is a local potential minimum at the center of the trap); this assures the harmonic motion of the charged particles inside the trap.

Single ions in electromagnetic traps offer many advantages for making precise measurements. The confinement times can be very long (on the order of weeks or months), which allows for many sequential experiments and/or very long experiments. The fact that the ion is trapped prevents collisions with walls. The trap is usually enclosed in an ultra-high vacuum (UHV) chamber, which reduces perturbing collisions with background gases. Also, we are very sensitive to the light emitted by the trapped ion, which allows for high-resolution observation of a particle that is less than one millionth of a meter in size. In addition, we are able to access the ion with lasers in order to cool its motional temperature to the μK range, which makes inhomogeneous broadening effects negligible. This is because even though performing many experiments on the ion allows us to look at the system as a distribution, the ion can be prepared in approximately the same state each time. Trapped ions are also ideal in experimental quantum optics and quantum information since they provide good realizations of two level systems. In our lab, we have assembled a linear ion trap for precision measurements and studies in quantum mechanics and quantum

information. In order to perform experiments we isolate our ion and manipulate its quantum mechanical state with stable lasers.

In Chapter 2 (Laser Interactions) I will describe the interaction between the ion and the laser beams. Since a laser beam incident on an ion can be viewed as a large electric field, its effect on the polarizable ion is very significant and the chapter will start off with a description of this physics. Because the main focus of this document is about how we can use light to probe an ion, I examine how lasers can interact with the ion. And because the linewidth is a fundamental characteristic of the ion as well as the quantity I propose to measure in the near future, I devote a section to describing its quantum mechanical properties and how to obtain a value of linewidth from experimental data. The linewidth of the ion can be altered by various mechanisms; our greatest concerns in the laboratory are linewidth-broadening due to the Doppler effect and the power broadening due to the incident lasers. These mechanisms, as well as their characterization, will be described. Finally, a crucial step in trapping an ion is ionizing the neutral atom. We discuss a technique to accomplish this called photoionization.

As mentioned before, we use the oscillating electric fields of a radio frequency (rf) linear Paul trap to confine the ion inside a low-pressure vacuum chamber and image the ion with a CCD camera that is positioned to capture a fraction of the light scattered by the ion. A thorough description of the set-up in our lab, the physics behind the instrumentation and the equipment used in our experimental setup is the focus of Chapter 3. This discussion follows the light along each beamline which terminates at the ion. I discuss the properties of the dye laser and the two fiber lasers and their frequency stability. The beams are directed into frequency doubling cavities: a description of second harmonic generation and the locking mechanisms of each cavity will be mentioned. Before reaching the trap, part of the beams goes into

diagnostics as well as devices that shift the frequency of the light. The light scattered by the ion is focused by a series of lenses onto a CCD camera, which is a method for detecting an ion in the trap.

Chapter 4 desribes calculations of the hyperfine splitting and Zeeman shifts (due to an external magnetic field) of the $1s^2 2s^2 2p^2 3s\ ^2S_{\frac{1}{2}}$, $1s^2 2s^2 2p^2 3s\ ^2P_{\frac{1}{2}}$ and $1s^2 2s^2 2p^2 3s\ ^2P_{\frac{3}{2}}$ states of $^{25}Mg^+$. A single energy level can be split into many sublevels. This is due to the fact that the charged particles that make up the ion interact with electromagnetic fields, as is apparent with the electric fields we use in trapping the ion as well as its manipulation with intense laser beams. What sets this "hyperfine" interaction apart is that the electromagnetic interaction is actually due to the different charges within the ion itself. Each of the ion's energy levels can be split into hyperfine sublevels related to the fact that the electrons and nucleus of the ion each have a net angular momentum which induces a magnetic moment. This property causes the nucleus and electrons to interact by way of the fields produced by the orbiting electrons. Although this interaction is not as strong as the interactions between the ion and the electromagnetic fields of the rf trap or laser beams, the shift in energy is non-negligible. The shifts due to the magnetic dipole moment and electric quadrupole moment are calculated and code is provided in an Appendix 1. The ion's energy level shifts due to the presence of a magnetic field – the Zeeman shift – are simultaneously calculated and the relationship between energy levels and applied external magnetic fields are plotted.

Finally, I propose to make a measurement of the range of light that will excite the ion to a specific energy level. I propose a linewidth measurement of $^{24}Mg^+$ using the $^2P_{\frac{3}{2}}$ level. We will obtain information on the linewidth by fitting the intensity of the scattered light as a function of the detuning to a well-known function: the Lorentzian. We will need to characterize and control the ion's movement and the intensity of the

laser because these effects make the uncertainty of the measurement larger. We will reduce the Doppler broadening by cooling the motional states of the ion. We will characterize the power broadening of the linewidth by using a range of powers to extrapolate to zero power. These preventative measures will allow for a more precise measurement of the natural linewidth of the ion. By fitting an experimental curve of scattered-light intensity vs. frequency to a Lorentzian, we can obtain information on the linewidth of $^{24}Mg^{+}$.

Chapter 2

Laser Interactions

Atoms are composed of a nucleus of positively charged protons and uncharged neutrons surrounded by negatively charged electrons. Interactions with electric fields induce a dipole moment which separates the opposite charges in the atom. Lasers are an intense source of coherent electromagnetic radiation; therefore, an atom in the presence of a laser beam interacts strongly with the electric field of this radiation. This interaction with the laser leads to transitions between and shifts in the energy levels of the atom.

To be more quantitative we can look at the quantum mechanical description of this interaction. We generally write the interaction between the atom and the laser as the dot product of the dipole moment of the atom induced by the electromagnetic field and the field itself. It is not immediately obvious how to write this expression for the interaction and so we start by writing a general Hamiltonian for an atom in the presence of a vector potential. The Hamiltonian can be written as :

$$H = \frac{1}{2m}(\vec{p} - e\vec{A})^2 - \frac{Ze^2}{(4\pi\epsilon_o)r} \quad , \tag{2.1}$$

where e is the charge of an electron, m is the mass of the particle, r is the separation between the electron and a point nucleus, $\vec{p}$ is the generalized momentum and $\vec{A}$ is the vector potential describing the intensity and polarization of the laser field (a more complete description can be found in (Bransden and Joachain 1983)). Because the current density of the electronic shells averages to zero we are able to use the Coulomb potential for Hydrogen ion.

We have separated the expression into two Hamiltonians describing (a) the atom in the absence of an electromagnetic field and (b) the atom in the presence of an electromagnetic field. We write the momentum in the familiar way, $\vec{p} = -i\hbar\vec{\nabla}$ and expand the square to get:

$$\begin{aligned} H &= H_o + H' \\ &= \frac{-\hbar^2}{2m}\vec{\nabla}^2 - \frac{i\hbar e}{m}(\vec{A}\cdot\vec{\nabla} + \vec{\nabla}\cdot\vec{A}) + \frac{e^2}{2m}\vec{A}^2 - \frac{Ze^2}{(4\pi\epsilon_o)r} \\ &\rightarrow \frac{-\hbar^2}{2m}\vec{\nabla}^2 - \frac{Ze^2}{(4\pi\epsilon_o)r} - \frac{i\hbar e}{m}\vec{A}\cdot\vec{\nabla} \end{aligned} \tag{2.2}$$

where we use the Coulomb gauge to impose the condition $\vec{\nabla}\cdot\vec{A} = 0$. This now implies that $\vec{A}$ and $\vec{\nabla}$ commute (using a wavefunction Ψ):

$$\begin{aligned} [\vec{A},\vec{\nabla}]\Psi &= \vec{A}\cdot(\vec{\nabla}\Psi) - \vec{\nabla}\cdot(\vec{A}\Psi) \\ &= \vec{A}\cdot(\vec{\nabla}\Psi) - (\vec{A}\cdot(\vec{\nabla}\Psi) + (\vec{\nabla}\cdot\vec{A})\Psi) \\ &= \vec{A}\cdot(\vec{\nabla}\Psi) - (\vec{A}\cdot(\vec{\nabla}\Psi) + 0) \\ &= 0 \end{aligned} \tag{2.3}$$

Also, we treat the absorption or emission of a single photon at a time so that $\vec{A}^2$ is negligible compared to the other $\vec{A}$ term in the Hamiltonian.

Focusing on the the interaction of the atom with the field we can rewrite some of the terms in the expression. We approximate the field to be a plane wave, $\vec{A} = A_o e^{-i\vec{k}\cdot\vec{r}}\hat{e}$, (where $A_o = \frac{1}{\omega}E_o$) since the wavefronts of the light will be approximately planar, given the size of the ion. Using the Heisenberg equation of motion for the momentum, we obtain:

$$\begin{aligned} -i\hbar\vec{\nabla} &= \vec{p} = m\frac{d\vec{r}}{dt} \\ &= m[\vec{r}, H] \end{aligned}$$

It is now useful to use H_o as the system Hamiltonian since we are working with the field as a perturbation and take the inner product of the above expression between the ground and excited states of the ion,$\langle\psi_e|$ and $|\psi_g\rangle$,

$$\begin{aligned}\langle\psi_e| - i\hbar\vec{\nabla}|\psi_g\rangle &= m\langle\psi_e|[\vec{r}, H]|\psi_g\rangle \\ &= (i\hbar)^{-1}m(\mathcal{E}_g - \mathcal{E}_e)\vec{r} \\ &= im\omega_{eg}\vec{r} \end{aligned} \tag{2.4}$$

Also, given the difference in size of the of the atom (on the order of $1\mathring{A}$) as compared to the wavelength of the laser field (optical wavelength $10^3\mathring{A}$), kr is very small. Expanding the exponential $e^{-i\vec{k}\cdot\vec{r}} = 1 + \vec{k}\cdot\vec{r} + \ldots$ we can replace the exponential with unity: this is called the dipole approximation.

The Hamiltonian can now be written as

$$\begin{aligned} H &= H_o + H' \\ &= H_o - \frac{i\hbar e}{m}\vec{A}\cdot\vec{\nabla} \\ &= H_o + (A_o\omega_{eg}\hat{e})\cdot(e\vec{r}) \\ &= E_o\hat{e}\cdot(e\vec{r}) \\ &= H_o + \vec{E}\cdot\vec{\mu} \end{aligned} \tag{2.5}$$

where $A_o = \frac{1}{\omega_{eg}}E_o$ since we are talking about the frequency of the field that is used to excite the transition $|g\rangle \rightarrow |e\rangle$ and $\vec{\mu} = e\vec{r}$ is the dipole moment of the atom. The above equation gives the interaction between the field and the electric dipole induced in the atom.

2.1 Linewidth

Conservation of energy implies that the frequency of light emitted from an atom decaying from a transition between excited state $|e\rangle$ and lower (energy) state $|g\rangle$ should be equal to $\omega_{eg} = \frac{(E_e - E_g)}{\hbar}$. This would result in a delta function at ω_{eg} on an intensity *vs* frequency plot of the light scattered from an atom decaying from an excited state $|e\rangle$ to lower-energy state $|g\rangle$. This, however, does not occur in experiment; the reason is related to the fact that the atom has a finite lifetime in the excited state $|e\rangle$.

The rate of spontaneous emission sets the time that the atom spends in its excited state. As the name implies, the emission is random. In the absence of an electromagnetic field the lifetime, one would think, should be infinite since there is no external perturbation to initiate decay to a lower energy level. In fact, quantum electrodynamics predicts a 'zero-point' field, where fields are non-zero even in the vacuum state (like the harmonic oscillator with a zero-point energy of $\frac{\hbar\omega}{2}$). A detailed calculation (Bransden and Joachain 1983) indicates that the excited state population decays exponentially over time for a given transition.

We can describe the lifetime of atoms in an excited state as follows: if we have a number, $n(t = 0)$ of the same atoms in the excited state $|e\rangle$ at time $t = 0$ then the number of atoms in the excited state at time t will be

$$n(t) = n(t = 0) \exp \frac{-t}{\tau} \quad , \tag{2.6}$$

where τ is the lifetime of the excited level of the atom. This is determined by (a) the transition rate for spontaneous emission, and (b) the number of states into which level $|e\rangle$ can decay, based on selection rules.

We can employ the Heisenberg uncertainty principle, $\Delta E \Delta t \geq \hbar$, to determine a minimum range of frequencies that the atom can absorb to excite from $|g\rangle$ to $|e\rangle$ or

emit to decay from $|e\rangle$ to $|g\rangle$. There is a non-zero probability that the light emitted will be in the range of energy $E_e - E_g$ or the frequency interval $\frac{1}{\hbar}(E_e - E_g)$ and as the uncertainty principle suggests, the decay time will be indeterminate proportional to this frequency range. The full-width half maximum (FWHM), in frequency space, of the function that is traced out by the intensity distribution is given by the frequency interval $\frac{1}{\tau_e} + \frac{1}{\tau_g}$, where τ_x is the lifetime of the level $|x\rangle$.

With this we can define a quantity, Γ, which is in units of angular frequency and is defined as the linewidth of the excited level:

$$\Gamma = \frac{1}{\tau_e} + \frac{1}{\tau_g} \quad . \tag{2.7}$$

The excited state population is exponential in time and in going from the time to the frequency domain we take the Fourier transform to get an expression for the number of excited atoms with respect to a certain frequency. The lineshape is written in the form of an intensity distribution (which is dependent on on the excited state population) and can be characterized by a Lorentzian (Bransden and Joachain 1983):

$$I(\omega) = Io\frac{(\frac{\Gamma}{2})^2}{(\omega - \omega_{eg})^2 + (\frac{\Gamma}{2})^2} \quad , \tag{2.8}$$

where I_o is some constant.

If the lower level $|g\rangle$ is the ground state of the atom, then, because there are no lower levels for this state to decay to, its lifetime is infinite. Therefore, expression becomes $\Gamma = \frac{1}{\tau_e}$ and is called the natural linewidth of state $|e\rangle$. The natural linewidth is the minimum width that the intensity distribution can have. It is commonly increased by mechanisms such as power broadening (which increases with the intensity of the laser beam) and Doppler broadening (due to the velocity distribution of moving atoms).

2.2 Power Broadening

The linewidth of a transition can increase if the intensity, I, of the incident laser beam has a much larger value than the saturation intensity, I_s, of the ion where $I_s = \frac{\pi hc}{3\lambda^3\tau}$ (Metcalf and van der Straten 1999). Here λ is the wavelength of the incident laser light and τ is the lifetime of the transition. The overall effect of power broadening is that the peak of the intensity profile saturates to some amplitude. This maximum amplitude of the lineshape is because the atom is in steady state, where the excitation rate equals the decay rate. In the frequency range near resonance, ω_o, the ion cannot increase its scattering rate (since it's in steady state), no matter how much we increase the intensity of photons incident on the ion. The wings of the intensity distribution, however, will continue to increase in amplitude with increasing intensity of the laser (until steady state is reached for the particular detuning $\delta\omega$) giving rise to a wider intensity profile.

In a more quantitative way, we define a saturation parameter, s, which describes how intense the incident beam is with respect to the saturation intensity of the ion, for a given intensity and detuning from the resonance of the transition (Metcalf and van der Straten 1999):

$$s = \frac{\frac{I}{I_s}}{1 + (\frac{2\delta\omega}{\Gamma})^2} \quad . \tag{2.9}$$

Here $\delta\omega$ is the detuning from resonance. The transition rate for the excited state will reach steady state as the intensity is increased (i.e. $s \gg 1$) and we define the scattering rate for the ion as (Metcalf and van der Straten 1999)

$$\begin{aligned} \gamma_s &= \gamma \frac{s}{2(1+s)} \\ &= \frac{\frac{I}{I_s}\frac{\Gamma}{2}}{1 + \frac{I}{I_s} + (\frac{2\delta\omega}{\Gamma})^2}. \end{aligned} \tag{2.10}$$

For large intensities we can write the scattering rate as:

$$\gamma_s = \left(\frac{\frac{I}{I_s}}{1+\frac{I}{I_s}}\right)\left(\frac{\frac{\Gamma}{2}}{1+\left(\frac{2\delta\omega}{\Gamma'}\right)}\right) \quad , \tag{2.11}$$

where $\Gamma' = \Gamma\sqrt{1+\frac{I}{I_s}}$ is the broadened linewidth. For the case $I \gg I_s$, γ_s saturates to $\frac{\Gamma}{2}$. Knowing this relationship, we are able to take the linewidths at various powers and extrapolate to zero power broadening.

2.3 Laser Cooling

The phenomenon of laser cooling is a seemingly contradictory one: photons add energy to an atomic system and it is a common to think that this would increase the effective temperature of the atom. But in fact we can use a laser beam to cool the ion – that is, slow its motional degrees of freedom. We will explain how this works in the following section.

2.3.1 Atomic Structure of Magnesium

The structure of the energy levels of $^{24}Mg^+$ does not have hyperfine splitting (see Figure 2.1). The structure of the $1s^22s^22p^63s\ ^2S_{\frac{1}{2}}$, $1s^22s^22p^63s\ ^2P_{\frac{1}{2}}$ and $1s^22s^22p^63s\ ^2P_{\frac{3}{2}}$ are shown.

The energy levels of $^{25}Mg^+$, on the other hand, are split due to the hyperfine interaction between the electronic and nuclear moments (see Chapter 4). The degeneracy of $1s^22s^22p^63s\ ^2S_{\frac{1}{2}}$, $1s^22s^22p^63s\ ^2P_{\frac{1}{2}}$ and $1s^22s^22p^63s\ ^2P_{\frac{3}{2}}$ states is lifted and split into $2F+1$ sublevels where F is the combined angular momentum of the ion's nucleus and electrons (see Figure 2.1). These sublevels are additionally shifted in the presence of an external magnetic field by the Zeeman effect.

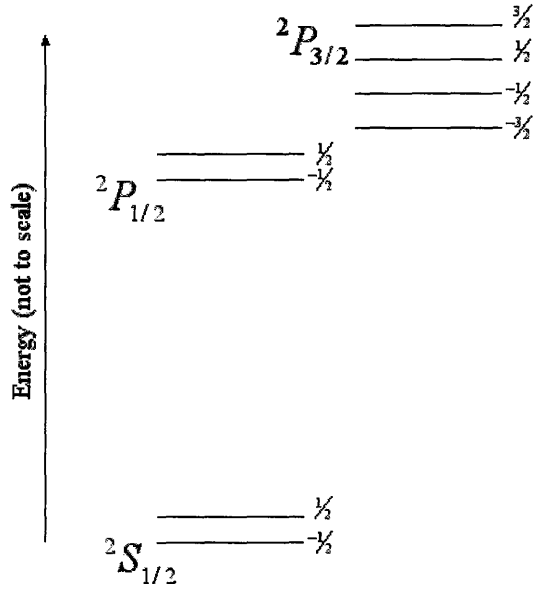

Figure 2.1: Energy level diagram of the $1s^2 2s^2 2p^6 3s\ ^2S_{\frac{1}{2}}$, $1s^2 2s^2 2p^6 3s\ ^2P_{\frac{1}{2}}$ and $1s^2 2s^2 2p^6 3s\ ^2P_{\frac{3}{2}}$ states of $^{24}Mg^+$

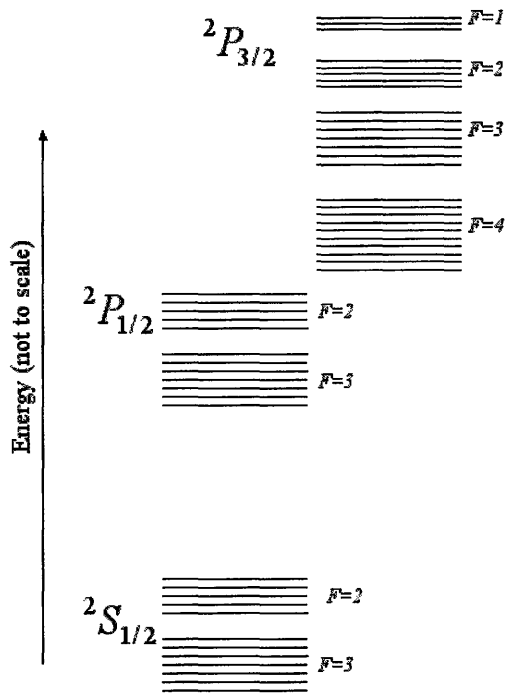

Figure 2.2: Energy level diagram of the hyperfine structure of $1s^2 2s^2 2p^6 3s\ ^2S_{\frac{1}{2}}$, $1s^2 2s^2 2p^6 3s\ ^2P_{\frac{1}{2}}$ and $1s^2 2s^2 2p^6 3s\ ^2P_{\frac{3}{2}}$ states of $^{25}Mg^+$

2.3.2 Cycling Transition

The ground state actually includes different sublevels into which the atom can decay due to the hyperfine splitting. In the case of $^{25}Mg^{+}$ we have 12 hyperfine levels in the ground state $^2S_{\frac{1}{2}}$. For illustrative purposes, we will look at two of the ground state hyperfine levels $|g_1\rangle$ and $|g_2\rangle$, connected to an unstable state $|e\rangle$ via a dipole transition. The two ground states are separated by one unit of angular momentum. If we are in a level $|g_2\rangle$ we can apply radiation of a circular polarization (σ^+) to add a unit of angular momentum to excite the level $|g_1\rangle \rightarrow$ level $|e\rangle$ transition. Since the $|g_1\rangle$ and $|g_2\rangle$ levels are so closely spaced in frequency, there is some finite probability to excite the level $|g_2\rangle \rightarrow$ level $|e\rangle$ transition. When the atom decays it can decay to levels $|g_1\rangle$ or $|g_2\rangle$: if it decays to level $|g_2\rangle$ it will be excited to level $|e\rangle$ again. It can also decay to level $|g_1\rangle$, where it will continue to excite and decay in the same transition $|g_1\rangle \rightarrow |e\rangle$. This is a cycling transition and occurs because we use circularly polarized light to excite the ion. The excited state will be one with an extra unit of angular momentum. We play this trick with an excited and ground sublevel that have the largest magnitude of angular momentum in their respective manifolds (and separated by one unit of angular momentum). Due to selection rules only the transition between these two sublevels will be driven. We often use the cycling transition of the ion as our detection transition since it produces many photons and the fluorescence is easily observed on our CCD camera.

2.3.3 Doppler cooling

Cooling the motion of the ion plays an essential role in trapped-ion experiments. If we wish to extract any meaningful information from a single ion, liinewidth-broadening effects on the transition measured must be kept to a minimum. Initially,

when the ion is trapped it is moving very fast because of heating in the oven (its velocity is very high even at room temperature). The Doppler effect causes the resonance frequency to be increased when the ion is moving away from the laser beam and decreased when the ion is moving toward the laser beam. This leads to Doppler broadening of the linewidth. Reducing the range of ion velocities through laser cooling reduces the Doppler broadening.

There are two extreme cases when looking at laser cooling: weak and strong binding regimes. In the case of a weakly bound atom, absorption occurs in $t \ll \frac{1}{\Omega_x}, \frac{1}{\Omega_y}, \frac{1}{\Omega_z}$, where Ω_i is the oscillation frequency of the atom for $i = x, y, z$ (Wineland and Itano 1979). When a photon is absorbed the atom receives a momentum kick $\vec{p} = \hbar\vec{k_l}$ in the direction of the laser (where $\vec{k_l}$ is the wave vector of the laser photon). After the absorption event, the atom will spontaneously emit a photon due to the fluctuations of the zero-point field and it will decay, on average, in the characteristic lifetime, τ, of the level. The photon will be emitted in a random direction and the momentum transferred, to first order, will average to zero. We are left with a net momentum transfer in the direction of the laser, which translates to change in velocity of (Wineland and Itano 1979)

$$\Delta\vec{v} \cong \frac{\hbar\vec{k_l}}{m_i} \quad , \tag{2.12}$$

where m_i is the ion mass. There is an overall cooling of the ion's motion if the direction of the ion's velocity opposes that of the laser. For a free atom one must have photons traveling toward the atom in all 6 directions with a range of frequencies such that $|\vec{k} + \Delta\vec{k}| < |\vec{k}|$, where $\Delta\vec{k}$ is the change in $\vec{k}$ of the absorbed and emitted photons and the net change serves to reduce the ion's momentum in the direction opposing the laser photon.

If we look at the process in second order, we notice that there is heating introduced into the system due to the recoil of the atom. Because the emission of photons is random, the momentum transfer can be viewed in momentum space as a random walk. And from conservation of energy, the limit on cooling has to be at least the recoil energy, E_r of the atom. To see this, we write the frequencies of absorption and emission on resonance (Wineland and Itano 1979):

$$\omega_a = \omega_o + \vec{k}_a \cdot \vec{v} - \frac{1}{2}\omega_o(\frac{|\vec{v}|}{c})^2 + \frac{E_r}{\hbar} \quad , \tag{2.13}$$

$$\omega_e = \omega_o + \vec{k}_e \cdot \vec{v'} - \frac{1}{2}\omega_o(\frac{|\vec{v'}|}{c})^2 - \frac{E_r}{\hbar} \tag{2.14}$$

where $\omega_o = 2\pi\nu_o$, $|\vec{k}_x| = \frac{\omega_x}{c}$, $\vec{v}$ and $\vec{v'}$ are the ground and excited state velocities. By conservation of energy and momentum the above equations are valid in emission and absorption processes to first order in recoil energy and second order in atom velocity.

The difference between the absorbed and emitted photon energies is:

$$\begin{aligned} \Delta E_p &= \hbar\omega_e - \hbar\omega_a \\ &= \hbar(\omega_o + \vec{k}_a \cdot \vec{v} + \frac{E_r}{\hbar} - \omega_o - \vec{k}_e \cdot \vec{v'} + \frac{E_r}{\hbar}) \\ &= -(\hbar\vec{k}_a \cdot \vec{v} + 2E_r) \end{aligned} \tag{2.15}$$

where we have omitted the term $\vec{k}_e \cdot \vec{v'}$ since the emitted photon wave vector will average to zero over many scattering events. We have neglected the $(\frac{|\vec{v}|}{c})^2$ terms because we are considering the non-relativistic limit (i.e. $|\vec{v}| \ll c$). If we look at it in terms of the atom: $\Delta E_i = (\hbar\vec{k}_a \cdot \vec{v} + 2E_r)$ and cooling will occur when $\hbar\vec{k} \cdot \vec{v} < -(2E_r)$, whereas heating results when $\hbar\vec{k} \cdot \vec{v} > -(2E_r)$.

The other regime for laser cooling is one where the atom is strongly bound, where absorption occurs on time scales $t \gg \frac{1}{\Omega_x}, \frac{1}{\Omega_y}, \frac{1}{\Omega_z}$. We will make an assumption that the oscillation frequencies in each direction are much greater than the linewidth of the transition but much less than the laser frequencies.

We can approximate the laser field incident on the atom as a plane wave along $\hat{i}$. This is because the spatial variation of the beam envelope occurs over a much larger distance than the size of the atom, resulting in wavefronts that are effectively planar. This laser field can be written as:

$$\vec{E} = E_o \sin(kx - \omega t)\hat{i} \quad , \tag{2.16}$$

where k and ω are the wave vector and frequency of the incident radiation, respectively; x describes the position of the atom. Since the atom is oscillating with some amplitude x_{max}, we can rewrite the position of the atom as:

$$x = x_{max} \sin(\Omega_x t) \tag{2.17}$$

where we are assuming no additional phase. The field now becomes

$$\vec{E} = E_o \sin[kx_{max} \sin(\Omega_x t) - \omega t] \quad . \tag{2.18}$$

This expression enables us to see that the atom is oscillating along the x-direction modulating the laser frequency ω by frequency Ω_x. The above equation can be written in terms of Bessel functions $J_n(kx_{max})$ (Wineland and Itano 1979), (Abramowitz and Stegun 1972) where kx_{max} is the modulation index. This has the effect of drastically changing the absorption spectrum: the atom will see a spectrum of carrier frequencies at ω_o and equally spaced frequencies that are Doppler shifted sidebands of $\omega_o + n\Omega_x$ (where $n = \pm integer$). These frequencies will have the width of the natural linewidth in the absence of any additional broadening and an amplitude of $J_n(kx_{max})$.

Being in the limit where Ω_x is much greater than the linewidth of the transition we can resolve the modulated sidebands. Cooling will occur if we irradiate the atom with light of frequency $\omega_o - n\Omega_x < \omega_o$, so that the lower-frequency sidebands are absorbed. The average frequency of the photons emitted will be approximately ω_o so

that the net effect is one that removes energy $n\hbar\Omega_x$ from the system. This treatment assumes the recoil energy is negligible.

2.3.4 Hyperfine Optical Pumping

First we have to prepare the ion into the cycling transition. We do this by optical pumping. Hyperfine optical pumping uses the polarization of light to populate specific closely spaced (in frequency) Zeeman sublevels. The technique is used when one is not able to spectrally resolve the sublevels. Being unable to resolve the hyperfine splitting is usually due to the finite linewidth of the laser and makes it very difficult to populate a specific level. The optical pumping used in our lab leads to the cycling transition (see Section 2.3.2) and occurs when we use circularly polarized light to excite the ion. If we use σ^+ polarized light, the interaction will add one unit of angular momentum to the atom and the excited state will have an extra unit of angular momentum. The excited state has a certain probability to decay down to a ground state by emitting σ^+, π or σ^- polarized light (depending on selection rules). Decaying to the ground state with σ^- light leaves the atom in the same state as it started in, while decaying with π and σ^+ results in an overall gain in angular momentum to the system. If we continue irradiating the atom, it will end up cycling between the ground sublevel with the largest magnitude of angular momentum and the excited state with one more unit of angular momentum – the cycling transition.

2.4 Ionization

When a neutral atom of magnesium travels through the deep potential well of the ion trap, its trajectory will not be disturbed by the electric field produced by the potential – the well is transparent with respect to the neutral atom. If, instead, we

use a magnesium *ion*, it will interact very strongly with the potential well and may be trapped. However, since the potentials that make up the trap are conservative, ions from outside of the trap accelerating toward its center will be expelled. The ions will experience a force due to these potentials and lose energy in climbing out of the well but will have gained an equal amount falling into the well in the first place. An analogous situation is a ball rolling in a bowl. If we take a ball and drop it into a bowl with any initial velocity, then the ball will gain some energy rolling down the side of the bowl and lose the same amount traveling up the other side. The result is that it will end up rolling right out of the bowl again with exactly the same speed as when it entered. This is obviously not an ideal situation for trapping. If, instead, we take the ball and release it in the bowl at some point along its side, the ball will roll up the other side of the bowl with, at most, enough energy to reach the same height on the bowl but not roll out. This is a crucial point that needs to be considered in the ionization of the atom. The idea is to ionize the atom inside the well so that it cannot leave its potential minimum, and therefore will be confined to the area inside the well.

The ionization can be carried out in two ways: (a) electron bombardment, an electron-atom collision process, and (b) photo-ionization, utilizing photons resonant with an ionizing transition of the atom. Both methods are used in the laboratory. Photoionization will be discussed here; for a discussion of both types of ionization see 3.6 We use a continuous-wave (CW) laser at 285nm to drive a two-photon transition through $3s^2\ {}^1S_o \longrightarrow 3s3p\ {}^1P_1$ (for a more detailed description see (Madsen, Balslev, Drewsen, Kjaergaard, Videsen, and Thomsen 2000)) in order to ionize our neutral magnesium (ionization energy $\tilde{7}$.5eV) with light. We use a single beam of π-polarized light to drive both transitions in the two-step ionization process. In this process, the neutral atom starts in the ground state and first is excited into an intermediate state

$3s3p\ ^1P_1$. Then the second step excites the transition 1 eV into continuum states ^1D_o or ^1S_o.

Chapter 3

Apparatus

There are many components beyond a source of ions and a trap that go into trapping ions for experiments. There are multiple lasers and beam lines as well as electronics. To be able to cool, ionize and manipulate the ions the light sources need to be precise as well as accurate. A vacuum chamber is utilized to keep the ion as isolated as possible. A layout of the laser table can be seen in Figure 3.1. In this section, I discuss how we realize our experimental setup as well as the theory of and use for each element in it.

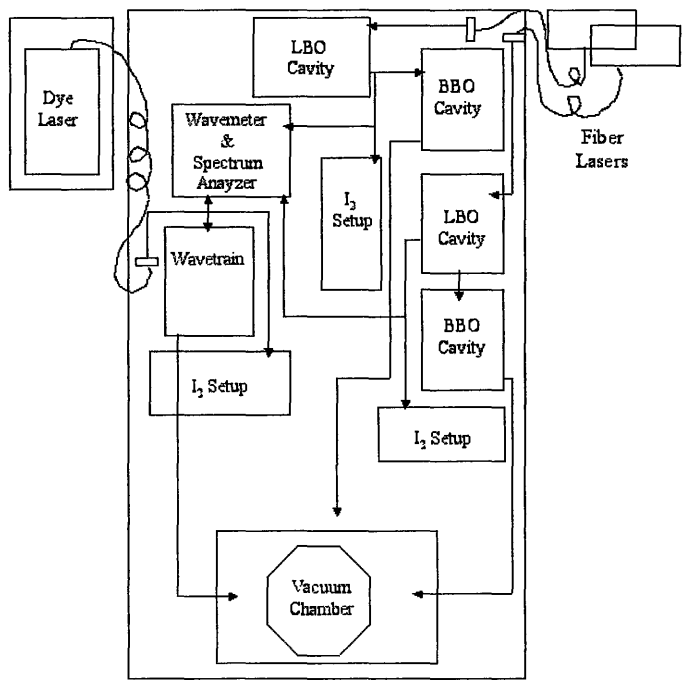

Figure 3.1: Schematic of the optical table and locations of the apparatus.

The beams used to cool, ionize and manipulate the magnesium ions inside the trap come from three different sources: the Coherent 699 dye laser and two Koheras fiber lasers (2W, 1W).

3.1 Dye Laser

The Coherent 699 dye laser (see Figure 3.2) is a traveling-wave laser that uses 5W-8W of a 10W Verdi diode-pumped solid state laser to optically pump the jet of ethylene glycol and Rhodamine-19 (the lasing medium). Part of the stimulated emission of light that comes from the jet is collected and directed by a bowtie configuration of four mirrors: three concave and one plane.

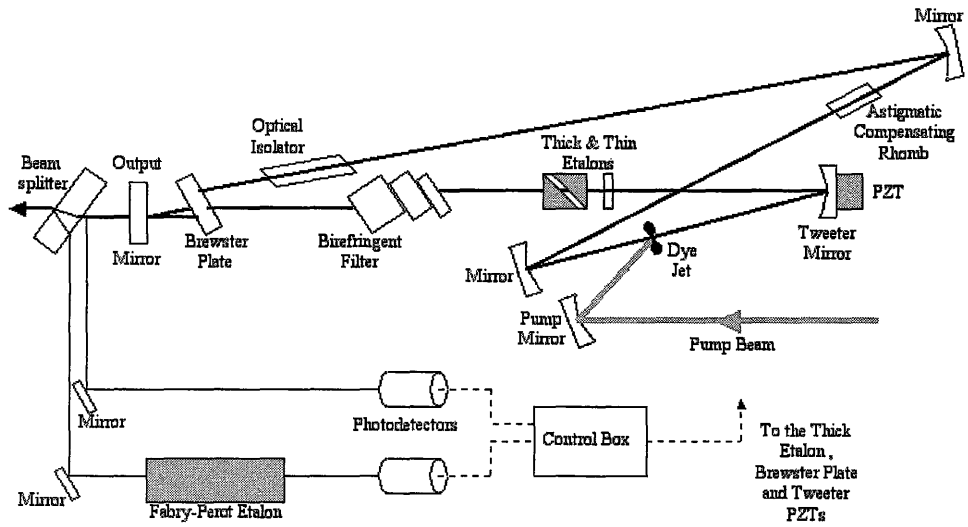

Figure 3.2: Schematic of the Coherent 699 dye laser cavity and reference cavity.

There are elements through which the beam travels in this configuration which act as wavelength selective elements: the birefringent filter and the intracavity assembly (ICA, containing the thin and thick etalons – see Figure 3.3, diagram courtesy of (Coherent Inc.)). The overall tuning range of the dye laser is tens of nanometers (for a given dye). In order to obtain a single lasing mode we must make sure that the mode we want is the least lossy. Because the stimulated emission of radiation from the laser is a highly non-linear amplification process, the least-lossy mode ends up winning in 'mode competition'. We use the birefringent filter and the ICA to introduce loss into the system. The least sensitive of these selective elements is the birefringent filter: its free spectral range (FSR) is on the order of 1THz. The thin etalon gives a higher resolution with an FSR on the order of 100GHz and the highest frequency selectivity is provided by the thick etalon with a FSR on the order of 10GHz (King 1982), (Duarte and Hillman 1990). The overlap of their transmittance peaks results in a single wavelength that has the least losses mode in the laser and is amplified through the non-linear process of lasing.

The birefringent filter is placed at Brewster's angle to the direction of propagation of the beam and uses three plates of polarization-sensitive quartz whose thickness ratio increase as powers (e.g. $4^0 : 4^1 : 4^2$) (Duarte and Hillman 1990). The plates are cut so that their surfaces are parallel to the optic axis of the quartz. This filter is similar to the Lyot filter design (Demtröder 2003), where the polarizers between waveplates are replaced by the waveplates cut at Brewster's angle. The waveplates can be rotated about the normal to their surface, thereby changing the angle between the laser polarization and the optic axis. For one particular wavelength the light will exit each plate with the same linear polarization as it entered. However, at other wavelengths, the polarization will be tilted and the light will therefore suffer losses in passing through all the Brewster-oriented elements in the laser cavity.

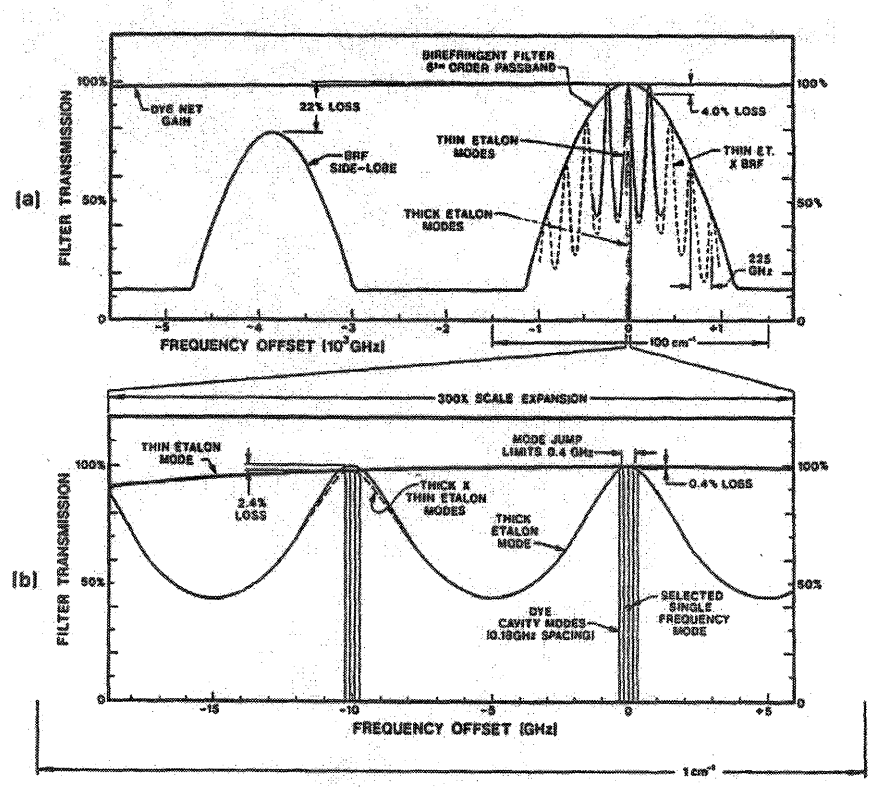

Figure 3.3: Transmission curves for the birefringent filter, thick etalon and thin etalon. This shows the wavelength selectivity of the dye laser (a). An enlarged section is seen in (b). Curves by Coherent Inc.

The thin etalon is more sensitive the birefringent filter. This etalon is simply a thin piece of glass. Tilting the glass makes the optical path length through the etalon longer and allows for selectivity.

The thick etalon consists of two thick pieces of glass that are reflection coated (~20%) on the outside. The inner surfaces are cut at Brewster's angle and separated by a distance that is adjustable by mechanical knobs as well as a piezoelectric transducer (PZT) that is electrically connected to the dye laser control box. The thick etalon is the most sensitive frequency selecting element of the three selective elements. The basic principle of this element is that the maximum transmission wavelength is a function of the distance between plates. For some wavelengths present in the beam, the phase differencebetween the transmitted waves becomes integer multiples of 2π. The reflected intesity becomes zero since the reflected waves destructively interfere for $\lambda = \lambda_m$, with an optical path length between successive wavelengths of $\delta = m\lambda$. We are able to change the transmission maximum λ_m by changing the distance between the plates.

3.1.1 Side Lock

In addition to frequency selection and tunability of the dye laser the stability of the chosen frequency is obviously of great importance. Dye lasers, in particular, are susceptible to large fluctuations in frequency. These fluctuations are due to the mechanical fluctuations of the laser cavity and the dye, which is moving very quickly in a high pressure jet stream. Mechanical fluctuations can change the resonance frequency of the laser cavity and it is therefore essential that a locking mechanism be used. The cavity is frequency stabilized with a side lock (King 1982), (Duarte and Hillman 1990). After the laser light travels through the output coupler a thick piece

of glass intercepts the beam. The two reflections from its front and back surfaces are used as monitor beams. One of the beams acts as a intensity reference and goes directly to a photodiode. The other beam travels through a Fabry-Perot etalon; it is this beam that is essential to deriving the signal that we eventually use. We lock to the side of etalon resonance, in the range where the etalon transmission is approximately linear. The reference beam and the transmittance curve of the cavity are subtracted from each other and the resulting electrical signal produces an error signal that is fed back to the laser. By adjusting the intensities of the reference beam with a variable attenuator, the difference in signals can be set to zero when the laser is tuned to the side of cavity resonance. We use the intensity of the reference beam as the DC offset to account for amplitude fluctuations, which can typically quite large in dye lasers. It is convenient to use a reference beam from the laser as the DC offset (instead of, say, an external electrical signal) because the intensity fluctuations of the laser will cancel when the two beams are subtracted.

The output of the dye laser is sent through a mode-matching lens into an optical fiber, used to transfer the beam from the dye laser table to the main optical table. The dye laser is on a separate table so the main optical table will not be affected by the large mechanical vibrations of the dye laser components and, most notably, the dye. Since the deflecton angle is multiplied by two every time the beam hits a mirror, the beam's translation from vibrations would be large if mirrors were used to transport the beam: obviously not an ideal situation when trying to trap a single ion in a volume of μm^3. To be more quantitative, if the vibrations deflected the beam by θ =0.01 degrees, then in 1m the beam would move shift by about 17.5μm and if there are 4 mirrors then this deflection is multiplied by 2^4 (provided all mirrors are 1m apart) which results in a total deflection of 2.75mm.

Once on the main table, the beam is then split into two by way of a polarizing beam splitter (PBS). Using fiber paddles, in which the fiber is wrapped around a series of moveable paddles, we can change the polarization of light coming out of the fiber and therefore change the amount of light that goes into each beam.

The vertically polarized beam gets split again: a wedge picks off about 4% of the beam for diagnostics and the rest goes to I_2 Doppler-free saturated absorbtion spectroscopy, which is used in an additional locking mechanism for the dye laser in an attempt to increase its frequency stability.

3.2 Diagnostics

The other beams that come from the vertically polarized beamline (reflected from the glass wedge) make their way to a Burleigh WA-1000 Wavemeter and a Thorlabs SA200-5A Scanning Fabry-Perot Interferometer.

The Wavemeter's function is to measure the wavelength of the incoming light to one part in 10^{-12}m (or 1pm). The Wavemeter is a travelling-cart Michelson interferometer as described in (Burleigh Instruments Inc. 2002), (Hall and Lee 1976): the beam travels through the entrance aperture where it is split by a 50/50 beamsplitter and each beam proceeds to a moving retro-reflector which recombines the beams back at the beamsplitter. The relative path lengths of the separated beams determines the intensity at the photodetector that is the next element that is reached by the beam. The back and forth movement of the retro-reflector makes the phase vary linearly (Doppler shifts occur due to the movement of the retro-reflector but the geometry cancels the shifts). The distance d that the incoming beam travels is related to the wavelength of the beam:

$$m\lambda = 4n_\lambda d \ , \tag{3.1}$$

where m is the number of fringes counted by the photodetector (PD), λ is the wavelength of the incoming beam and n is the refractive index of air. At the same time there is an internal reference helium-neon (HeNe) laser that is sent through the travelling interferometer and the fringe signal is sent to a seperate PD and compared with the signal from the PD of the incoming beam:

$$\lambda = (\frac{m_o}{m_\lambda})(\frac{n_\lambda}{n_o})\lambda_o \quad , \tag{3.2}$$

where the subscripts o and λ denote the reference and incoming beam quantities, respectively.

The other beam diagnostic is a Thorlabs SA200-5A spectrum analyzer, which is a high-finesse Fabry-Perot etalon. This allows for the determination of structures in the spectral characteristics of the incoming beam. The etalon acts as a narrow bandpass filter and by varying the distance between the mirrors in the etalon with a PZT we are able to change the postion of the pass-band in frequency space. Using the known free spectral range (FSR) of the etalon, we can measure relative frequency changes in the input beam. This device is used for drift-rate measurements of the laser as well; because we know the FSR of the etalon we can calibrate the x-axis when looking at the transmitted intensity versus frequency (provided the etalon is stable). Therefore we can see how the frequency shifts over a given time (to account for possible drifting of the etalon itself, a stable laser may be used as a reference). Linewidth measurements can also be performed using this etalon. Since the etalon has a fixed linewidth determined by its losses, fixing the spacing between the mirrors in the cavity and tuning the frequency of the laser to the side of the cavity's resonance curve (where the slope is approximately linear) means that there will be observable change in frequency if the intensity changes. We can thus convert intensity changes into frequency changes (like the sidelock of the dye laser, Section 3.1).

3.3 Doppler-Free Saturated Absorption Spectroscopy

We need some stable frequency standard to which to lock our laser. Because the I_2 molecule has many well-defined transitions within the range of 560nm to 570nm, we can use it as a reference for our lock. In Doppler-free saturated absorbtion spectroscopy, we observe the signal from hyperfine components of the iodine transitions and use the signal in a feedback loop to the electronics of the dye laser (more detail on the subject is found in (Petrich 1994)). We use a series of laser beams that travel through a glass cell containing I_2 vapour to excite the transitions. Externally scanning the frequency with a function generator (that outputs a triangle wave with a peak to peak voltage of 5-10V) allows us to scan over the entire transition width of approximately 43MHz. The range of frequencies that is scanned is set by adjusting the Scan Width adjustment on the 699 control box. Since the I_2 is in a room-temperature vapour cell, the Doppler shifts broaden the width of the transition. To further examine this, we can see that if a molecule has a transition frequency ω_o when at rest, then when the molecule is moving, its new transition frequency, and therefore the frequency of light the atom will absorb, is given by:

$$\omega = \omega_o + \vec{v} \cdot \vec{k} \quad , \tag{3.3}$$

where $\vec{v}$ is the velocity of the molecule and $\vec{k}$ is the direction of propagation of laser beam (to first order in $\frac{v}{c}$). Even for a large detuning of the laser, $|\omega - \omega_o| \gg 0$, there will be some atoms that will be on resonance with the incoming laser beam because there is a large velocity distribution in a gas at room temperature.

We now approximate our molecules to be two level systems. We pass a laser beam through the vapour cell with $\vec{k} = (0, 0, k_z)$. Given that the resonance of the molecule is ω_o at rest, if the laser has a frequency ω, only molecules with the velocity $\vec{v}$ (from

Equation 3.3), will be resonant with the beam out of the entire velocity distribution. In fact, a range of velocities interact strongly with the laser. This range is determined by another broadening mechanism: saturation of the transition. This broadening is given by

$$\Delta\omega = \Gamma\sqrt{1+\frac{I}{I_s}} \quad , \tag{3.4}$$

where Γ is the natural linewidth of the transition and I_s is the saturation intensity of the molecule (which are inherent properties of the particular species). The laser beam drives a population transfer between the ground and excited state, for this narrow velocity class, $\Delta v_z \sim \frac{\Delta\omega}{c}$. This gives rise to absorption of the laser beam and this absorption results in a decrease in intensity of the transmitted beam.

Using an intense pump beam (that saturates the molecule) traveling with $\vec{k} = (0, 0, k_z)$ and an overlapping counterpropagating weak probe beam (whose intensity is much less than saturation), $\vec{k} = (0, 0, -k_z)$, we can extract information from the probe beam. If we keep the frequencies of both beams fixed, the pump beam will interact very strongly with molecules whose velocity is such that they absorb light of $\omega = \omega_o + v_z k_z$, whereas the probe beam will interact with the velocity class that will absorb $\omega = \omega_o - v_z k_z$. The result is a large increase in the excited state population of the velocity class interacting with the pump beam and a smaller increase in population of the exicted state population for the velocity class interacting with the probe beam. If we scan over the transition, the probe beam will give a Doppler-broadened curve when looking at the absorption of the beam as a function of frequency of the laser, except when the frequency of the laser is close to resonance frequency ω_o.

Near resonance, $(v_z k_z \approx -v_z k_z \approx 0)$, the probe signal will have a decrease in ground state population since the pump beam will be interacting with the same velocity class. The pump beam saturates the transition so that the probe beam cannot

interact with the molecules, decreasing their absorption of this beam. Looking at the probe signal as a function of frequency one would see a dip at $\omega = \omega_o$ in the Doppler broadened peak. We also create a weak reference beam that travels parallel to the probe in the same direction and use this purely Doppler-broadened signal to extract a transtion peak that is not Doppler broadened. This is achieved by subtracting the probe signal (Doppler broadened curve with a dip) from the reference signal (Doppler broadened curve only), this resultant signal should look like a flat line with a peak centered at $\omega = \omega_o$.

We realize this in the laboratory as follows (see Figure 3.4): the beam goes through a double-pass 80MHz AOM, which doubles the frequency shift and provides zero angular deflection (since the deflection upon travelling though one way will be negated when it travels back through the other way). The first order beam is then sent through an angled piece of glass. The reflected beams are used as weak probe and reference beams and are sent through the vapour cell. The beam that continues through the glass is the pump beam and is sent through an 80MHz acousto-optic modulator (AOM) for the purpose of frequency modulation.

The AOM works using Bragg diffraction. A PZT that expands and contracts at 80MHz creates a travelling sound wave at that same frequency. The PZT is driven with a sinusoidally varying voltage. The wavelength of the sound wave in the crystal is on the order of the wavelength of light being diffracted. If the incoming beam of light satisfies the condtion,

$$\theta_B = \frac{\lambda}{2\Lambda} \quad , \tag{3.5}$$

where Λ = sound wave spacing, then diffraction will occur. The intensity of the first-order diffracted beam is maximized when the incident beam and the first order beam are symmetric about the sound wave. The frequency of the diffracted beam is shifted

because there is a Doppler shift experienced by the light as the travelling acoustic wave travels across it. The shift is equal to the frequency of the acoustic wave; the sign of the Doppler shift is determined the sound wave's direction with respect to the laser beam (the shift is positive if the sound wave and laser beam are travelling toward each other and negative when they have components propagating in opposite directions).

We use an 85kHz sine wave to frequency modulate the 80MHz sound wave in the AOM. The probe and reference beams illuminate two photodetectors and the subtracted (electrical) signal is sent to a lock-in amplifier. The purpose of the lock-in is to increase the signal to noise ratio of the peaks and change the phase between the modulating signal and signal from the photodiode so that they are out of phase with each other to give dispersion curves instead of peaks. We then lock to the point where the dispersion curve crosses zero: the feedback signal is sent to the control box of the dye laser to make the appropriate change in frequency.

3.3.1 Iodine Spectrum

As mentioned earlier, we need a stable frequency standard to which to lock our laser. The I_2 molecule has many well-defined transitions in the optical range and more specifically, in the range near the $^2P_{\frac{1}{2}}$ transition in magnesium. We will use the 1W fiber laser (repumper see Section 3.5) to drive the $^2P_{\frac{1}{2}}$ transition and use a hyperfine component of the 1599 iodine transition line (Luc and Gersrekorn 1978) as a reference for our lock. I obtained a spectrum of iodine and calibrated the x-axis in terms of frequency in MHz.

To obtain the spectrum we monitored the signal from the lock-in amplifier while the laser PZT was scanned over a range of 0-50V. This voltage range corresponds to a

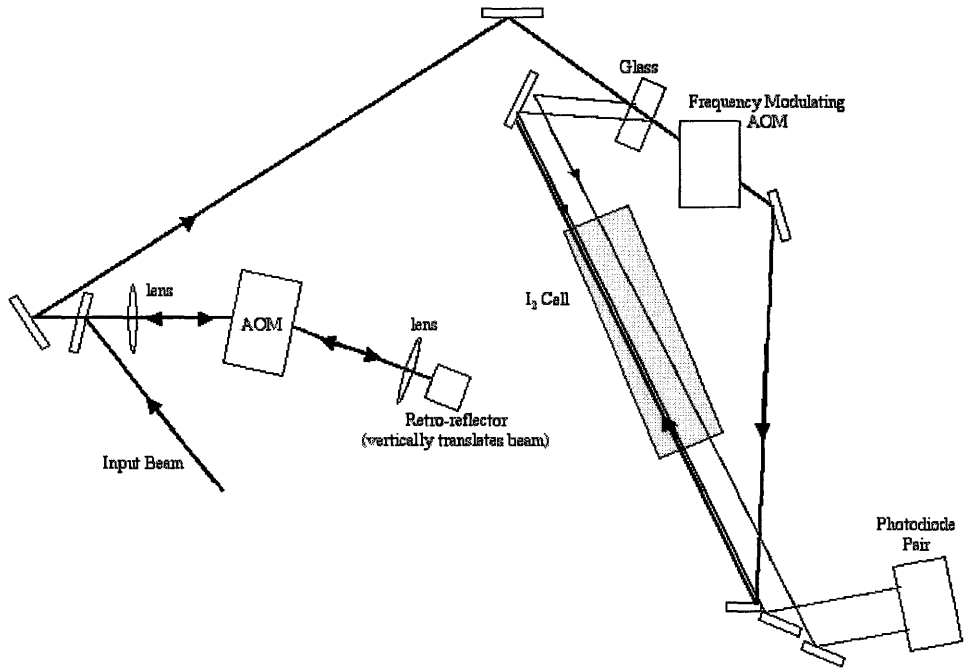

Figure 3.4: Schematic of Doppler-free saturated Iodine Spectroscopy setup.

2.5GHz shift in frequency of the fiber laser (since 1V applied to the PZT corresponds to a specified 10pm shift in wavelength). A Labview program aquired 5000 data points (with 100 averaged samples per point) with a voltage increment of 0.01V. The data that is output from this program can be plotted as lock-in signal versus voltage. Since we require knowledge of the peak locations relative to each other in terms of frequency (MHz), calibration of the x-axis is needed. The relationship between the voltage applied to a PZT and the frequency change in the laser due to its expansion (or contraction) is, in general, not linear. In order to find out what this relationship is we need to sample how the laser frequency changes as a function of voltage using a stable reference.

The dye laser was input into the spectrum analyzer to act as a stable reference compared to the fiber laser since the drift of the optical spectrum analyzer was a concern. The laser was locked (by hand) to an iodine hyperfine transition that is a known distance from the $^2S_{\frac{1}{2}} \rightarrow^2 P_{\frac{3}{2}}$ transition in $^{24}Mg^+$. Using a Textronics digital oscilliscope the traces of the spectrum analyzer (with dye laser and fiber laser input) were taken at a number of voltages (where $\Delta V \approx$ 5-10V). Representative plots of these traces can be seen in Figures 3.5 and 3.6. The FSR of the spectrum analzyer's Fabry-Perot cavity is known to be FSR=1.59GHz (measured by Jason Nguyen) which was measured over timescales which made drift negligible. Using a known frequency separation (461.54MHz (Leibfried 2006)) between hyperfine components of the 1833 iodine transition (Luc and Gersrekorn 1978) at 559.271nm, the shift of the peak locations were monitored. This known frequency seperation was used to obtain the frequency seperation of the recurring peaks on the spectrum anlyzer output.

Knowing the FSR we are able to use the spacing between the dye and fiber laser peaks at known voltages and obtain a voltage to frequency conversion for the voltage

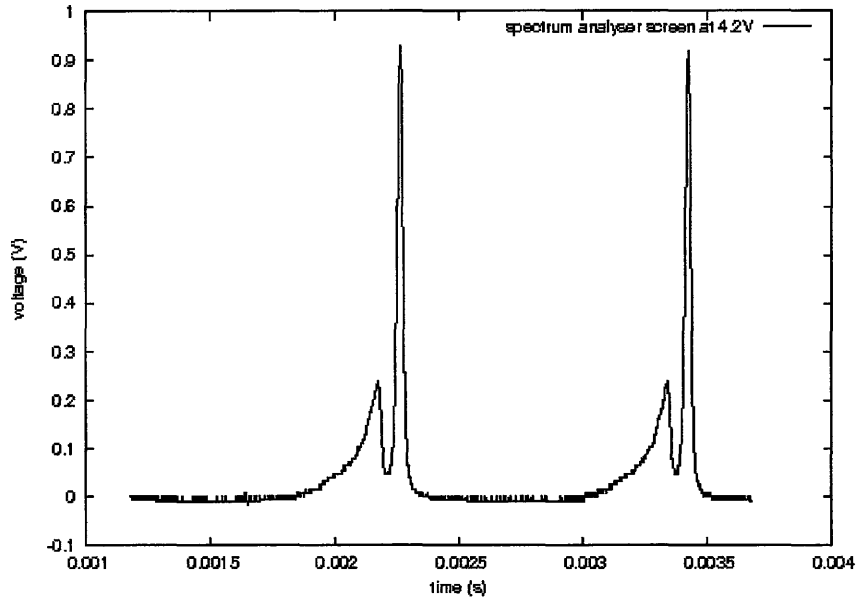

Figure 3.5: Representative plot of the screen on the oscilliscope when scanning laser frequency. Plot is taken with 4.2V applied to PZT. High peaks are the dye laser and smaller peaks are the fiber laser.

sweep in the saturated iodine spectrum. These separations were plotted as a function of voltage (see Figure 3.7) and fit to a quadratic function

$$\begin{aligned} f(V) &= aV^2 + bV + c \\ &= 0.0614898V^2 + 38.0281V - 45.3555. \end{aligned}$$

The residuals of this function are plotted in Figure 3.8. The rms of the residuals was found to be less than 1% of the frequency range; therefore this fit was used in the calibration. A linear fit to the data points was made but since the residuals of the quadratic fit were slightly lower we decided to use the quadratic fit in the calibration. The asymptotic standard error in the coefficients of the fit are a =36.53%, b =3.414% and c =34%. Gnuplot was used to fit and plot all data. The calibrated iodine spectrum is shown in Figure 3.9.

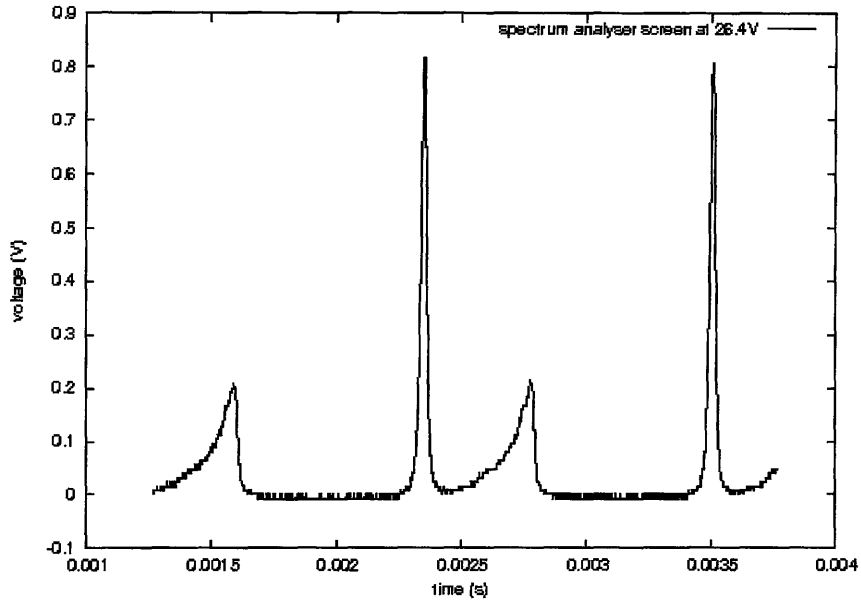

Figure 3.6: Representative plot of the screen on the oscilliscope when scanning laser frequency. Plot is taken with 26.4V applied to PZT. High peaks are the dye laser and smaller peaks are the fiber laser.

3.4 Wavetrain Doubling Cavity

The output from the dye laser is transmitted through a fiber and travels through a PBS, as mentioned earlier. The vertically polarized light is sent to the iodine spectroscopy setup and diagnostics while the horizontally polarized beam goes to the Spectra-Physics Wavetrain frequency doubling cavity (see (Spectra Physics)). The frequency of the laser is doubled in a beta-barium borate (BBO) crystal. The beam is mode-matched using two mirrors and two lenses that matches the mode of the beam to that of the cavity. Through a beamshifter, which is a piece of glass that serves to translate the beam, the light enters the cavity (resonator block) through a spherical mirror (M1) (see Figure 3.10). From here it passes through the crystal and reaches a second spherical mirror (M2), passes through a prism and gets bent to return to the first spherical mirror. The cavity elements are aligned such that the mode of the cavity is TEM_{00}. The mode of the cavity is monitored by scanning the prism with

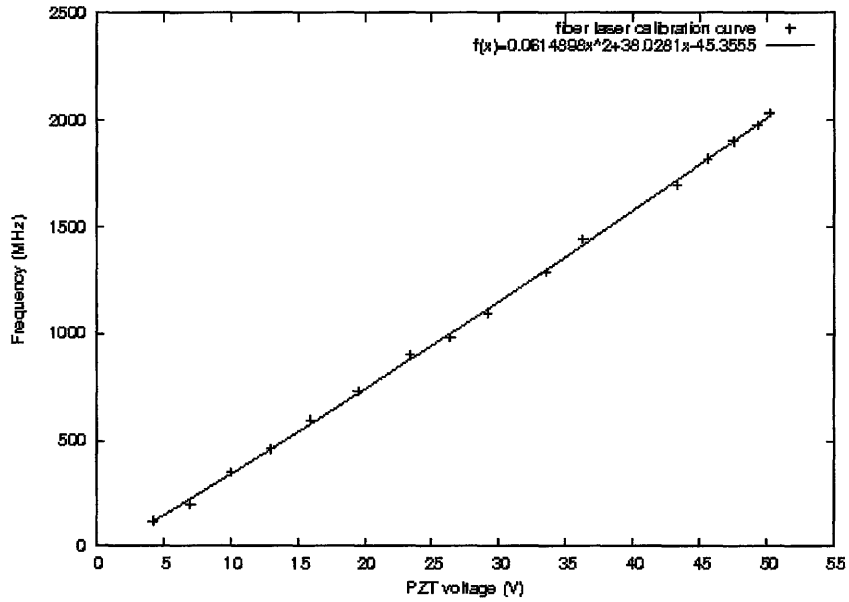

Figure 3.7: Plot of peak separation (fiber laser and reference dye laser) versus voltage applied to the PZT. The dots represent actual data points and the line is a quadratic fit: $f(V) = aV^2 + bV + c = 0.0614898V^2 + 38.0281V - 45.3555$. Plot and fitting done with Gnuplot; asymptotic standard error: a =36.53%, b =3.414% and c =34%.

a PZT and looking at the signal due to the green light on a photodetector that is located downstream of the spherical mirror (M2).

3.4.1 Pound-Drever-Hall Frequency Stabilization

The cavity is kept resonant with the Pound-Dever-Hall locking scheme (Figure 3.11). This scheme incorporates the doubling cavity in order to monitor the relative frequency changes of the incoming light. The signal from the cavity is used to decrease the cavity fluctuations by feeding back to the PZT of the cavity. This frequency stabilization method is especially powerful since it can distinguish the intensity changes due to off-resonant frequency fluctuations from intensity fluctuations of the laser itself.

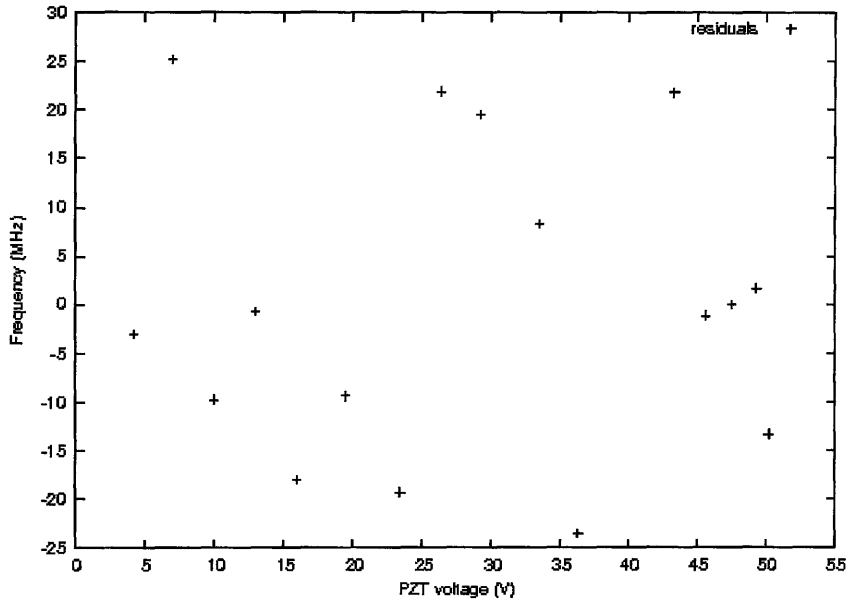

Figure 3.8: Plot of the residuals of the quadratic fit ($f(V) = aV^2 + bV + c$) versus PZT applied voltage, used in calibrating the x-axis of the iodine spectrum.

The light incident on the cavity is first sinusoidally dithered with a Pockel's cell at a frequency, Ω_s, that is larger than the bandwidth of the doubling cavity. This gives rise to sidebands of spacing Ω_s and a carrier frequency ω (which is the only frequency in the sideband spectrum within the bandwidth of the cavity). We use a photodiode to look at the beam that comes from the input coupler; this beam is composed of the light reflected from the cavity and the light that leaks through the input coupler from inside the cavity. The sidebands of frequency $\omega + \Omega_s$ and $\omega - \Omega_s$ are always reflected (since their frequecies are outside of the bandwith of the cavity) and are used as a phase reference.

The photodiode is used in converting the phase information to intensity information by sending the photodiode's electrical signal, which is the beating of the carrier and the side bands, to a mixer. The mixer uses the frequency at which the beam is modulated and beats it against the signal from the photodiode to obtain a signal that is fed back to the cavity to keep it resonant. When the cavity is on resonance,

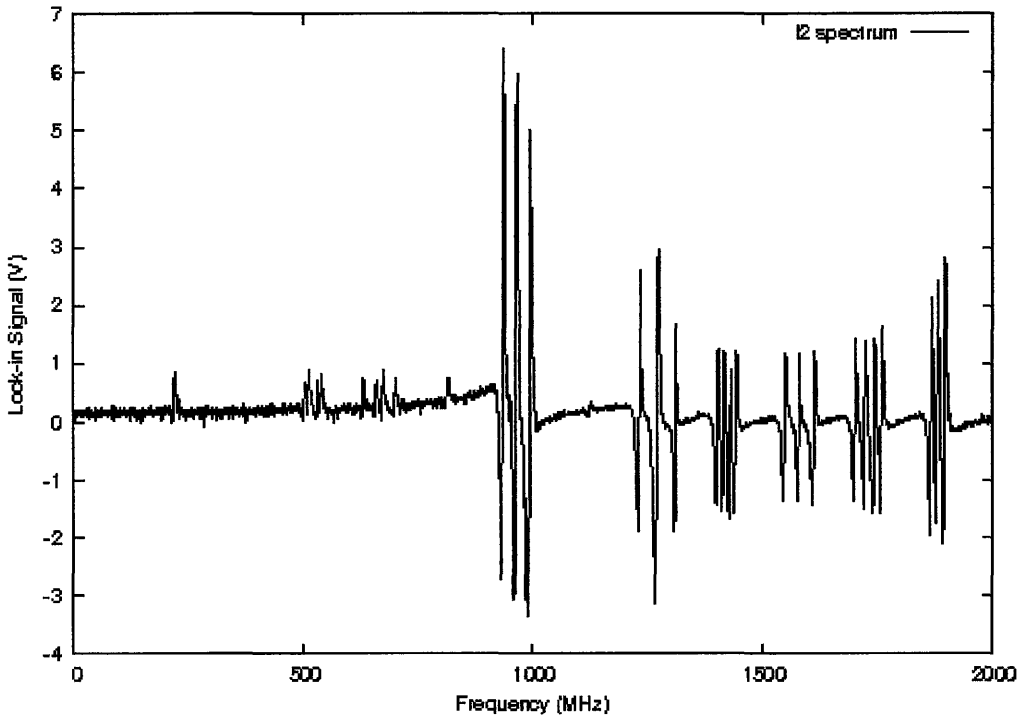

Figure 3.9: Spectrum of Iodine, (I_2) with calibrated x-axis in MHz.

the light at the carrier frequency that leaks out through the input coupler will be in phase with the carrier and sidebands that are reflected. In this case the intensity will be a maximum and the error signal will be zero. When the cavity is off-resonance the carrier light that leaks through the input coupler has aquired a phase shift and the intensity decreases. The error signal that is fed back to the PZT will be non-zero.

The lock-in acts as a mixer that allows us to look at the signal of the side-bands beating against the reflected carrier. The sign of this signal tells us what side of resonance we are on. When this is sent to a PID (proportional-derivative-integral) loop and fed back to the cavity, the resultant error signal is applied to the PZT and it moves to bring the cavity back to resonance. For a more detailed treatment, refer to (Black 2001).

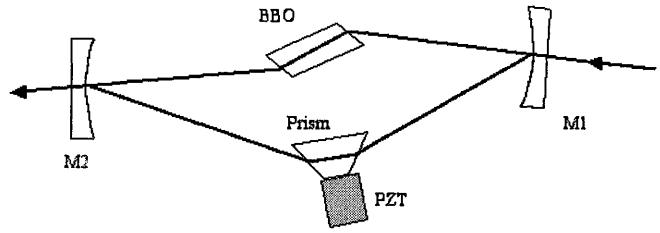

Figure 3.10: Schematic of Spectra-Physics Wavetrain frequency doubling cavity.

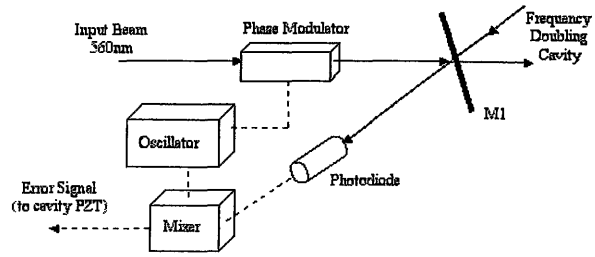

Figure 3.11: Schematic of Pound-Drever-Hall frequency stabilization setup used to stabilize the Wavetrain frequency doubling cavity.

3.4.2 Second Harmonic Generation

The Wavetrain uses a birefringent crystal to generate second harmonic light from the input beam. An intense electromagnetic field in the presence of a dielectric crystal drives nonlinear processes. Such processes can generate a beam of light that is twice the frequency of the incoming beam.

In general, a light field will exert a force on the outer electrons of the atoms in the crystal, which results in a variation of the electric polarization (see (Hecht 2002)). To hone in on the most significant physics we'll write a scalar equation for the polarization (the polarization, of course, is a vector quantity that may – in the case of nonlinear effects – point in a different direction than the applied field)

In a weak light field the electric polarization is linearly proportional to the field that is being applied:

$$P = \chi E \ , \tag{3.6}$$

where P is the polarization, χ is the electric susceptibility coefficient and E is the applied electric field. In strong light fields, as is common with the use of lasers, the polarization is no longer a linear function of the electric field. Therefore, the above equation is invalid for strong fields. The polarization can be expressed as a power-series expansion in the electric field:

$$P = \chi_1 E + \ \chi_2 E^2 \ + \ O(E^3) \ , \tag{3.7}$$

Since the linear susceptibility term, χ, is much larger than the higher order susceptibility terms, it can be seen that only at strong electric fields does the second order

term become non-negligible. For a light field $E = E_o \sin(\omega t)$ going through a dielectric crystal, we can write the polarization as:

$$P = \chi_1 E_o \sin(\omega t) \quad + \quad \frac{\chi_2}{2} E_o^2 (1 + cos(2\omega)) \quad + \quad O(E^3), \tag{3.8}$$

Here we can see that when a strong enough light field exerts a force on the outer electrons of the atoms in the crystal, a variation in a component of the electric polarization of the light that is at twice the frequency of the incoming light field will result.

Quantum mechanically, frequency doubling is a two-photon process. Two photons of fundamental frequency ω combine to make a single photon of frequency 2ω.

In frequency doubling in a crystal of finite length, dispersion plays a major role. Dispersion is the dependence of frequency/wavelength on the refractive index of the crystal. At each point where the second harmonic light is generated, both fundamental and second harmonic are in phase. If the refractive indices and therefore the phase velocities of the fundamental and second harmonic are not equal, however, the second harmonic wave generated at some length down the crystal will be out of phase with second harmonic light generated elsewhere. The result is destructive interference – that is, the intensity of the second harmonic is reduced.

In the case where the indices of refraction are exactly the same $n_\omega = n_{2\omega}$, the maximum amount of second harmonic light is produced; a result of constructive interference. This can be achieved by a process called angle tuning. The fundamental beam is a linearly polarized ordinary wave (polarized perpendicular to the principle plane) and the second harmonic is a linearly polarized extraordinary wave (polarized parallel to the principle plane). Because the ordinary beam is perpendicular to the optic axis of the crystal the index of refraction is not dependent on angle and traces out a circle with respect to angle with the optic axis (see Figure 3.12). The extraordinary

ray, on the other hand, traces out an ellipse of different $n_{2\omega}$ values as a function of the angle with the optic axis. Therefore, there will be some specific angle θ where the circle and ellipse intersect and the indices are the same. When the laser makes the angle θ to the optic axis of the crystal $n_\omega = n_{2\omega}$ and the maximum intensity of generated second harmonic light results.

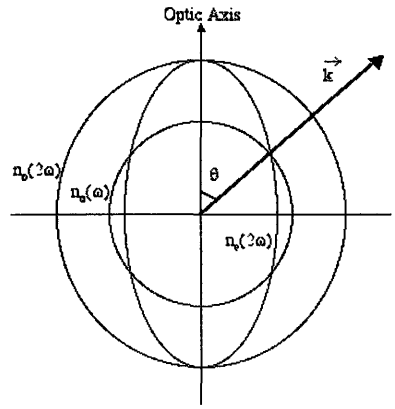

Figure 3.12: Indices of refraction of the ordinary wave ($n_o(\omega)$ and $n_o(2\omega)$) and extraordinary wave ($n_e(2\omega)$) with respect to angle, θ, from the optic axis.

In the Wavetrain, ultraviolet (UV) light is transmitted through the second spherical mirror (M2) in the cavity, which is highly transmissive around 280nm. From the spherical mirror, (M2) the beam is sent through a cylindrical mirror and an anamorphic prism pair. These elements serve to compensate for the ellipticity and astigmatism of the beam (meaning they are capable of changing the waist position and size of the beam in one plane). The beam is elliptical and astigmatic due to "walk-off". Walk-off is the effect of the polarized extraordinary ray interacting with the anisotropic crystal. The result is a loss of of spatial overlap during propagation at

some angle (the walk off angle) which is simple the angle between $\vec{k}$ and the Poynting vector (which defines the direction of energy transport). In effect, the useful interaction length and thus the conversion efficiency can be limited, and the spatial profile of product beams may be broadened and the beam quality reduced.

After the lens and prism pair, the now-circular beam is sent out of the Wavetrain exit aperture and through lens that gives the optimal beam size through the next element: an acousto-optic modulator (AOM).

AOMs are used in our applicatons to switch the beam on/off or shift the frequency of the incoming light. In this particular section of the beam line the AOM is used to deflect the beam in such a way that the beam's frequency is shifted by 200MHz and its trajectory is one that passes through the center of the ion trap; when the AOM is off, the beam does not reach the ion trap.

After the AOM, the beam is then sent through a series of mirrors and lenses that bring it to the center of the ion trap with an appropriate waist size.

3.5 Fiber Lasers

Two Koheras A/S Boostik fiber lasers that operate in the infrared produce the beams used for the cycling transition ($^2S_{\frac{1}{2}} \rightarrow^2 P_{\frac{3}{2}}$) and to drive the $^2S_{\frac{1}{2}} \rightarrow^2 P_{\frac{1}{2}}$ transition which can be used as a 'repumper' used concurrently during Raman cooling.

Because of our need to have lasers with both power and frequency stability to drive the ions into their different excited states we use fiber lasers. The Koheras fiber lasers are constructed of a fiber with a ytterbium-doped inner core that acts as the active gain medium. Using ultraviolet (UV) illumination, a Bragg grating is etched onto the fiber; this gives the fiber laser it's narrow linewidth. We can also use the grating to change the wavelentgh by small increments (~picometers). The fiber is

pumped with a 980nm semiconductor laser. Then by use of an internal amplifier the signal is increased to produce 2W and 1W beams of 1118nm and 1121nm light, respectively, with a linewidth of less than 40kHz.

The lasers are able to tune over a small range of wavelengths by two mechanisms: varying the temperature of the fiber and/or changing the voltage across the piezoelectric transducer (PZT) that is connected to the fiber. The largest change in wavelength can be achieved by changing the temperature and therefore the refractive index of the fiber; for every degree Celsius change we change the wavelength by 11pm. The temperature can be tuned from room temperature to around 35-40 degrees. By making small changes in the spacing in the Bragg grating period we can increase or decrease the wavelength. This is achieved by changing the voltage applied to a PZT that is connected to the fiber which serves to stretch the fiber and thus the integrated gratings. By applying a voltage in the range between 0V and 200V we can expect a maximum of 20pm change in wavelength.

3.5.1 LBO and BBO Doubling Cavities

The single-mode fibers that are used to carry the light emitted from the lasers are mounted at a four inch beam height and sent through optical isolators, which prevents light from being fed back through the fiber into the laser and causing damage to the amplifier. The beams are then sent to frequency doubling cavities with a four mirror bowtie configuration. These cavities were designed in-group by Jason Nguyen and JiaJia Zhou. Two cavities were made for each laser: one to double infrared to green and a subsequent cavity to double green to ultraviolet.

The 1120nm light goes to a frequency doubling cavity which uses a lithium borate (LBO) crystal to halve the wavelength to 560nm (green). Phase matching (see section

3.4.2) is accomplished by heating the crystal to around 100 degrees Celsius rather than by using angle tuning. The cavity uses two spherical concave mirrors of radius r =75mm that are located on either side of the 7mm long crystal, and two plane mirrors ($r = \infty$) to close the cavity. A PZT is mounted to one of the spherical mirrors in order to scan the cavity (FSR= 439MHz) and lock the cavity. The input coupler is one of the flat mirrors (see Figure 3.13) and has a reflectivity R=98%. The spherical mirror without the PZT functions as the output coupler and is highly reflective at the fundamental (infrared) and highly transmissive at the second harmonic (green).

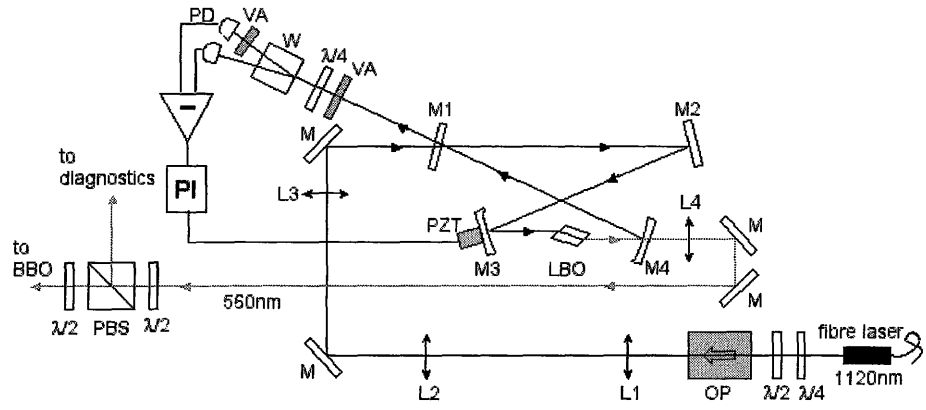

Figure 3.13: Schematic of frequency doubling cavity using LBO and Hänsch-Couillaud frequency stabilization scheme for the cavity. [Definition of terms in figure: OP= optical isolator; W = Wollaston prism; VA= variable attenuator; PD= photodiode; PI=proportional and integral gain for the feedback loop; M's and L's are mirrors and lenses] Figure courtesy of JiaJia Zhou.

The 560nm light goes to a frequency doubling cavity, by way of mode matching optics. This doubling cavity uses a beta barium borate (BBO) crystal to halve the

wavelength to 280nm in the ultraviolet. In order to phase match, the crystal is angle tuned (see section 3.4.2). This cavity uses two spherical concave mirrors of radius 75mm that are located on either side of the 7mm crystal, and two plane mirrors ($r = \infty$) to close the cavity. A PZT is mounted to one of the spherical mirrors in order to scan the free spectral range of the cavity (FSR= 435MHz) and is used in locking the cavity. One of the flat mirrors functions as the input coupler (see Figure 3.14) and has a reflectivity R=97%. The spherical mirror without the PZT functions as the output coupler, which is highly reflective at the fundamental (green) and highly transmissive in the second harmonic (ultraviolet).

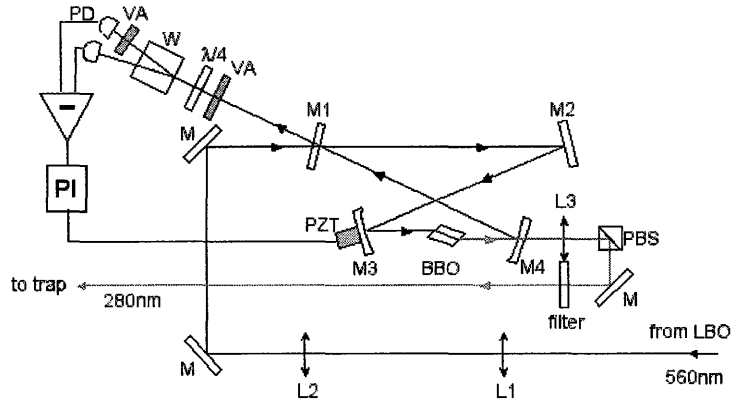

Figure 3.14: Schematic of frequency doubling cavity using BBO and Hänsch-Couillaud frequency stabilization scheme for the cavity.[Definition of terms in figure: W = Wollaston prism; VA= variable attenuator; PD= photodiode; PI=proportional and integral gain for the feedback loop; M's and L's are mirrors and lenses] Figure courtesy of JiaJia Zhou.

3.5.2 Hänsch-Couillaud Frequency Stabilization

We lock the aforementioned cavities using the Hänsch-Couillaud method (Hansch and Couillaud 1980). In this scheme we monitor the beam that is reflected from the input coupler of the doubling cavity (see Figures 3.13 and 3.14). The cavity requires horizontally polarized light since it contains a polarization sensitive element: the doubling crystal cut at Brewster's angle. Since the input coupler is slightly transmissive, some of the light circulating in the cavity leaks out of the cavity and mixes with the beam that is reflected at the input coupler. Even though the cavity requires horizontally polarized light, a small amount of vertically polarized light is added to determine the size of the error signal. When the cavity is resonant the horizontally polarized light sees a low-loss cavity and the reflected and transmitted beams destructively interfere resulting in zero intensity. When the cavity is off-resonance, the transmitted light wave experiences a frequency dependent phase shift upon its transit around the cavity. The addition of the transmitted, phase-shifted, horizontally polarized beam to the reflected (horizontally *and* vertically polarized) beam produces an elliptically polarized beam with an ellipticity depending on detuning from resonance. By decomposing and separating this elliptically polarized beam into its linear components we are able to monitor changes in the polarization of the component beams.

The reflected beam from the input coupler is sent through a $\frac{\lambda}{4}$ plate oriented at 45 degrees and then through a Wollaston prism (which is a polarizing beam splitter). The $\frac{\lambda}{4}$ plate takes purely circularly polarized light and decomposes it into two orthogonal linear polarizations while the PBS separates these beams into two equal-intensity beams. The beams that have been split illuminate two photodiodes. The resulting electrical signals are then sent to a differential amplifier. When the cavity is off-resonance, the polarization is elliptical and so the light is unequally split on the analyzer. The electrical signal from the differential amplifier is therefore nonzero.

The sign is determined by which side of resonance the cavity is on. The resulting error signal is then filtered and sent to the PZT of the doubling cavity, which moves the mirror the appropriate amount to keep the cavity on resonance. The stable-frequency UV beams now make their way to the trap.

All of the stable, frequency-doubled beams (from the 2W and 1W fiber lasers and the dye laser) are then combined on a polarizung beam-splitter (PBS) on their way to the trap. They are combined on the PBS to ensure overlap at the center of the trap. The beams proceed through the anti-reflection (AR) coated fused silica windows of the vacuum chamber, by way of focussing optics, and subsequently into the center of the trap.

The vacuum chamber has a pressure of around 5×10^{-11}torr. This is achieved by use of a constantly running ion pump and a titanium sublimation pump (TSP) that we fire off on a daily basis. The chamber, ion pump and TSP were all baked in an oven at a temperature of 200 degrees Celsius to desorb water and other contaminants from the stainless steel of the chamber and the other materials that make up the trap electrodes, ion sources, electron guns, electrical wires, etc..

3.6 Ion Source

There are three main items inside the chamber: ^{24}Mg and ^{25}Mg ovens, electron guns, and the rf trap.

The magnesium ovens are constructed using tantalum tubing of inner diameter of 0.86mm and a wall thickness of 0.08mm with a length of close to 1cm. A hole of 1mm diameter is poked in the middle of the long axis, while allows the magnesium to exit the vessel. The tube is then pinched off at one end to a length of about 20mm, filled with magnesium foil, and pinched on the other side. The ends are folded once

so that they are oriented away from the hole. These folds are then spot welded to stainless steel rods that are connected to electrical feedthroughs. The ovens each have their own feedthrough for passing current and share a common ground; this is how we heat the magnesium so that it sublimates. By using thin-walled tubing we create a large resistance and when current passes through the tube, the tube heats and consequently heats the magnesium. A 1cm×1cm×1cm box made from stainless steel shim having a 1mm hole is also placed over top of the oven to direct the beam to the center of the trap.

The ionization can be carried out in two ways: (a) electron bombardment, an electron-atom collision process, and (b) photoionization, utilizing photons resonant with an ionizing transition of the atom. Both methods are used in the laboratory. Photoioniztion was mentioned in Section 2.4, and a comparison of the two methods is given below.

Electron impact ionization involves many high-energy electrons bombarding a beam of magnesium. A filiment of thoriated tungsten is heated resistivly and due to thermionic emission electrons are given off. The electron guns consist of a coiled length of thoriated tungsten 0.25mm diameter wire. The wire is coiled to maximize its surface area and is spotwelded to two stainless steel rods connected to electrical feedthroughs. When a current of 0.5A is passed through the wire thermionic emission occurs and electrons are given off in all directions. In order to direct them toward the trap and give them a high energy (so that the impact of the electrons on the neutral atoms will be enough to remove an orbital electron) we use a stainless steel wire grid held at a voltage of 15V. This supplies the electrons with an enery of 15eV, and because the ioinzation energy of magnesium is <10eV there is more than enough energy to facilitate ionization. The electron coil and the grid are aligned so that the beam of electrons goes through the center of the trap; the ovens also direct their

neutral magnesium beams in this manner and the intersection of each of the beams is at the center of the trap. This facilitates ionization of the magnesium at the center of the trapping region. Photoionization may also be used (see 2.4).

Electron bombardment uses an electron gun that causes outgassing in the vacuum chamber as the filament heats up and heats the chamber as well. This will produce other atoms and molecules in the chamber. These contaminants have the potential to collide with trapped ion to remove it from the trap or prevent it from being trapped in the first place. Also, the vast quantity of electrons given off can charge the dielectric surfaces in the chamber, which can affect the trapping fields (when the electrons come into contact to the conductive material in the chamber, they will flow to ground).

Photoionization is an alternative to electron bombardment that is cleaner in the sense that there are no additional contaminants as a result of trying to photoionize. Photoionization is a very selective method of ionizing magnesium. Because the laser is tuned to be resonant with the ionizing transitions in neutral Mg, it ionizes only the isotope that we want while leaving other isotopes, atoms of background gas and existing ions unaffected.

3.7 Radiofrequency Trap

The radio frequency ion trap uses a combination of static and sinusiodally varying voltages applied to stainless steel rods and tubes to create an area of minimum potential surrounded by high potentials (time-averaged). If we were to use a static parabolic potenial:

$$\Phi(x,y,z,t) = U_o \frac{1}{2}(\alpha x^2 + \beta y^2 + \gamma z^2) \quad , \tag{3.9}$$

the Laplace condition, $\Delta\Phi = 0$ would imply that $\alpha + \beta + \gamma = 0$ and it can be seen that there would be no local potential minimum in three dimensions for a static field. If we add a time-dependent part that varies sinusoidally with an rf frequency Ω_T :

$$\Phi(x,y,z,t) = U_o\frac{1}{2}(\alpha x^2 + \beta y^2 + \gamma z^2) - V_o\cos(\Omega_T t)\frac{1}{2}(\alpha' x^2 + \beta' y^2 + \gamma' z^2) \quad ,(3.10)$$

it is possible to choose an rf drive frequency and voltages such that the above potential can produce stable, approximately harmonic motion to trap the ions in all directions.

A more quantitative description of the potentials used to trap or charged particle uses the pseudopotential approximation described by (Kapitsa 1951). We will set U_o to zero to focus on the dynamic trapping. Using our sinusoidal potential we can write the equation of motion for the trapped ion in one dimension:

$$\begin{aligned} F &= eE = e\frac{-\partial\Phi}{\partial x} \\ &= eV_o\cos(\Omega_T t)\alpha' x = m\ddot{x} \qquad (3.11) \\ \ddot{x} &= [\frac{eV_o\alpha'}{m}\cos(\Omega_T t)]x. \qquad (3.12) \end{aligned}$$

We can separate the motion into a slow motion with a large amplitude and fast motion with a small amplitude; we refer to these as secular motion (x) and micromotion (x_μ), respectively . The total motion of the ion is simply the sum of each component: $X = x + x_\mu$ (King 1999),

$$\ddot{x} + \ddot{x}_\mu = [\frac{eV_o\alpha'}{m}\cos(\Omega_T t)](x + x_\mu) \quad . \qquad (3.13)$$

If we assume $x_\mu \ll x$ and $\ddot{x} \ll \ddot{x}_\mu$, this equation becomes

$$\ddot{x}_\mu = \frac{eV_o\alpha' x}{m}\cos(\Omega_T t) \quad . \qquad (3.14)$$

We can obtain x_μ by integrating the above equation with respect to time:

$$x_\mu = \frac{eV_o\alpha'}{m}\frac{(-1)}{{\Omega_T}^2}\cos(\Omega_T t)x \quad . \qquad (3.15)$$

Substituting all terms into equation 3.13 we now obtain an expression for the secular motion:

$$\begin{aligned} \ddot{x} + \ddot{x}_\mu &= [\frac{eV_o\alpha'}{m}\cos(\Omega_T t)](x + x_\mu) \\ \ddot{x} + [\frac{eV_o\alpha'}{m}\cos(\Omega_T t)]x &= [\frac{eV_o\alpha'}{m}\cos(\Omega_T t)][1 + \frac{eV_o\alpha' x}{m}\frac{(-1)}{{\Omega_T}^2}\cos(\Omega_T t)]x \\ \ddot{x} &= -(\frac{eV_o\alpha'}{m\Omega_T})^2 x \cdot \frac{1}{2} \\ &= -(\frac{eV_o\alpha'}{\sqrt{2}m\Omega_T})^2 x \end{aligned} \tag{3.16}$$

where we have averaged the squared micromotion term, oscillating at trap frequency Ω_T, to $\cos^2(\Omega_T t) \rightarrow \frac{1}{2}$. Finally we have an expression for the secular motion, and from this we can infer the secular frequency:

$$x = \cos(\frac{eV_o\alpha'}{\sqrt{2}m\Omega_T}t) \tag{3.17}$$

$$\omega_s = \frac{eV_o\alpha'}{\sqrt{2}m\Omega_T} \tag{3.18}$$

Our trap uses the linear Paul trap design (see Figure 3.15) as opposed to the spherical quadrupole design. We use four rods whose centers lie on a square (looking along the axial direction). Tubing of approximately the same size as the rods is placed over one diagonal pair of rods. We apply a static DC voltage to these tubes. One pair of diagonal rods is held at rf ground while the other pair has a voltage that is driven at Ω_T applied to it.

In practice we use an rf drive frequency of $\frac{\Omega_T}{2\pi} = 25$MHz, an rf voltage of 150V and a static voltage of 30-40V. The rods are 0.79mm in diameter with a length of 56mm. The distance between the rod centers is 2mm; along the rods the tube electrodes are spaced by 3mm with a length of 10mm (see picture in Figure 3.16). The resulting axial frequency of the trap is $\omega_z \simeq 0.6$MHz.

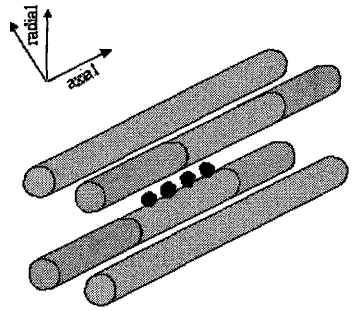

Figure 3.15: Schematic of a linear Paul trap. Rf voltages are applied to the rods (light gray) and a DC voltage is applied to the tubing around the rods (dark gray). Diagram is not to scale.

3.8 Imaging System

The ion fluorescence is the means by which we can (a) detect the presence of ions in the trap and (b) measure the internal state of the ion. The UV imaging system used for collecting the fluorescence is shown in Figure 3.17. Simply put, the imaging system consists of two sets of lenses with an aperture between them. Photon detection is carried out using a UV-sensitive charge-coupled device (CCD) camera. The first optical element (L1) is an objective lens (Mitutoyo M Plan UV 20x) with numerical aperture 0.36 and focal length of 10mm. It provides a short focal length with a relatively long working distance of 15mm. The fluorescence from the ion is collimated by the objective and focused by a 50mm focal length lens (L2) (CVI laser BICX-25.4-50.6-UV). This second lens is also used to correct the spherical aberration introduced by the vacuum window (also referred to as the viewport: Ceramaseal

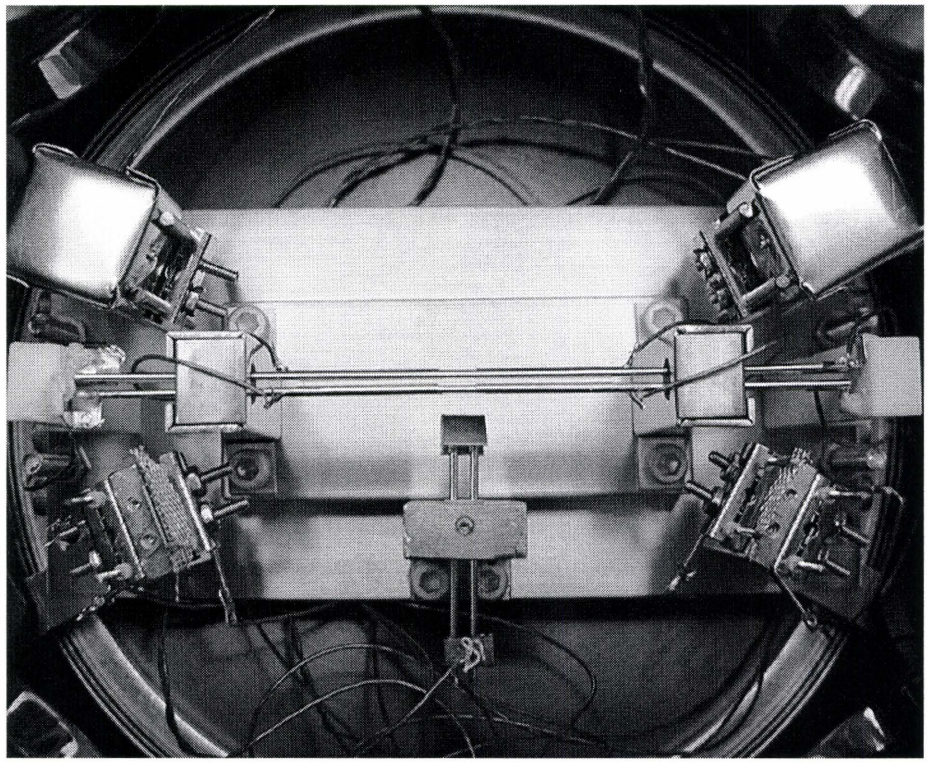

Figure 3.16: Picture of the rf trap in the vacuum chamber. The trap is surrounded by two electron guns and two shielded ovens. Photograph by JiaJia Zhou.

11466-01-CF, 3.2mm thick fused-silica window, AR coated at 280nm). An adjustable aperture is placed near the ion image produced by L2, and is used to filter out the background light and scattered light from the electrodes. After passing through this aperture, the collected fluorescence is focused onto the CCD camera by another lens (L3), which consists of two 150mm focal length plano-convex lenses (Newport SPX025). The magnification of the first set of lenses (L1 and L2) is 5 and that of the second set is 8, for an overall magnification of 40.

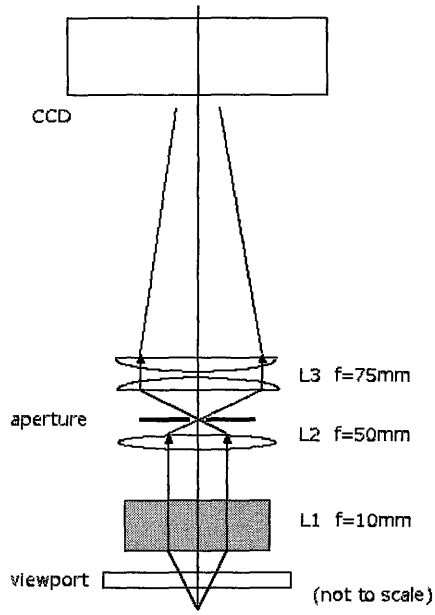

Figure 3.17: Schematic of imaging system for the CCD camera.

The CCD camera used in the experiment is from Andor Technology (iXon DV887ECS-UVB). The camera has single-photon capability and a specified 35% quantum efficiency at wavelength 280nm. The camera has a square image area 8.2 mm× 8.2mm with 512 × 512 pixel resolution. The camera is invaluable as it gives us the ability to align the imaging system with respect to the trap electrodes and form an image of the trapped ion.

The detection system collects light in a 0.417 steradian solid angle. Taking into account the ion's dipole radiation pattern, only 4.86% of the fluorescence will be collected. The loss due to various optics elements is estimated to be 60% and the camera has a specified quantum efficiency of 35% at 280nm. Taking all of these factors into account, the overall detection efficiency of the system was calculated to be about 1%.

Chapter 4

Hyperfine Interaction

Atoms possess magnetic properties which create further structure in their energy levels. There is a magnetic moment $\vec{\mu_l}$ that is associated with the orbital angular momentum $\vec{l}$, of the charged electrons about the nucleus. Classically, we can think of an electron in a circular orbit as a current moving in a circular path. This produces a magnetic dipole field and it follows that the electron possesses a magnetic dipole moment (Woodgate 1983),

$$\vec{\mu_l} = -\frac{g_l \mu_B}{\hbar} \vec{l} \ , \tag{4.1}$$

where g_l is the gyromagnetic ratio (which is the ratio of the magnetic dipole moment to the angular momentum and is experimentally determined) and μ_B is the Bohr magneton. The magnetic moment $\vec{\mu_s}$ is associated with the intrinsic quantity spin, $\vec{s}$, of the electron (Woodgate 1983):

$$\vec{\mu_s} = -\frac{g_s \mu_B}{\hbar} \vec{s} \ . \tag{4.2}$$

These magnetic moments are oriented (anti-) parallel to each other such that the two configurations of the magnetic moments have slightly different energies from the interaction between the spin and orbit of the eletrons. This difference produces a shift in energy with a magnitude that is dependent on the relative orientation of the magnetic moments. This is known as the fine structure splitting of the atom. There is an additional splitting of the fine structure energy levels that is a result of the

interaction of the electronic and nuclear fields. This "hyperfine splitting" is orders of magnitude smaller than the fine structure and will be topic of the current chapter.

4.1 Hyperfine Interactions of Particles

The interaction between a magnetic field $\vec{B}$ and the magnetic moment of the atom (due to its orbital electrons) leads to a splitting of energy levels. Analagous to the electronic magnetic moments, the magnetic moments of the atom, $\vec{\mu}_I$ and $\vec{\mu}_J$, are associated with the total angular momenta of the nucleus, $\vec{I}$, and electrons $\vec{J} = \vec{s} + \vec{l}$. The total nuclear angular momentum is a fixed quantity since we are only treating the case where the nucleus is in its ground state. The total angular momentum of the atom is given by the sum of the nuclear and electronic momenta:

$$\vec{F} = \vec{I} + \vec{J} \ , \tag{4.3}$$

that can take on values $(I + J), (I + J - 1), ...|(I - J)|$. For closed electronic shells $\vec{J} = 0$, so only the valence electrons will contribute to the total electronic angular momentum for most atoms. These magnetic moments can only orient themselves in discrete directions relative to the quantization axis, which can be set by the direction of any ambient magnetic field. The nucleus has electromagnetic multipole (2^k-pole) moments. The interaction of these moments with the valence electrons' electric and magnetic fields at the nucleus are the cause of hyperfine splitting. The multipoles that do not vanish (because they keep the mirror symmetry of the nucleus with respect to its equatorial plane) are magnetic moments with odd k and electric moments with even k (Kopfermann 1958). The magnitude of the magnetic multipole moments decrease more rapidly as a function of k than the electric multipoles. Therefore only the magnetic dipole and the electric quadrupole will addressed in this chapter.

4.1.1 Magnetic Dipole Interaction

The total angular momentum of the nucleus has a magnetic moment associated with it, that is

$$\begin{aligned} \vec{\mu}_I &= g_I' \mu_B \vec{I} \\ g_I' &= g_I \frac{m_e}{m_p} \end{aligned} \tag{4.4}$$

where g_I, the nuclear g factor, accounts for the structure of the nucleus. Assuming a point nucleus, we can describe the nuclear magnetic moment, $\vec{\mu}_I$, interacting with the magnetic field, $\vec{B}_e$ created by the valence electrons by the Hamiltonian:

$$H = -\vec{\mu}_I \cdot \vec{B}_e \ . \tag{4.5}$$

We can treat this interaction as a small perturbation since the hyperfine interaction is so much smaller than the fine structure. Nuclear coordinates are used for $\vec{\mu}_I$ and electronic coordinates for $\vec{B}_e$. Using the time-averaged magnetic field $\vec{B}_o$ that is produced by the electrons, we can write the perturbation as(Woodgate 1983), (Kopfermann 1958):

$$\begin{aligned} \Delta H_D &= -\mu_I B_o \cos(\vec{\mu}_I, \vec{B}_e) \\ &= AIJ\cos(\vec{I}, \vec{J}) \\ &= A(\vec{I} \cdot \vec{J}) \ , \end{aligned} \tag{4.6}$$

where $\vec{I} \cdot \vec{J} = \frac{F^2 - I^2 - J^2}{2}$ and $A = \frac{\mu_I B_o}{IJ}$ are experimentally determined. The product $\vec{I} \cdot \vec{J}$ can be expressed in terms of standard angular momentum operators: $\vec{I} \cdot \vec{J} = I_z J_z + \frac{1}{2}(I_+ J_- + I_- J_+)$; this expression is used in the perturbation since we use the m_I, m_J basis for the hyperfine calculation (as opposed to the m_F basis). Our perturbation is written in this way because the magnetic interaction couples I and

J, so the magnetic field produced by the electrons is a quantity proportional to the total electronic angular momentum.

Treated quantum mechanically we replace F^2, I^2, J^2 by $F(F+1), I(I+1), J(J+1)$, and our perturbation is

$$\Delta H_D = A[I_z J_z + \frac{1}{2}(I_+ J_- + I_- J_+)] \quad . \tag{4.7}$$

4.1.2 Electric Quadrupole Interaction

The electric quadrupole interaction is the next higher-order, non-negligible multipole term, and it produces a smaller perturbation than the interaction due to the magnetic dipole moment as outlined in (Woodgate 1983), (Kopfermann 1958). This interaction is due to the finite spatial extent of the nucleus. Consider the electrostatic interaction of the electrons and protons:

$$H = \frac{-e^2}{4\pi\epsilon_o|\vec{r}_e - \vec{r}_n|} \quad , \tag{4.8}$$

where $\vec{r}_e$ and $\vec{r}_n$ are the position vectors of the electron and proton, respectively. By summing over all protons in the nucleus and all surrounding electrons, we gain the total electrostatic interation of the atom. The electric quadrupole moment, Q_o, is a measure of the deviation of the nuleus from a spherical charge distribution, $\rho(r)$, that is symmetric along an arbitrary axis (oblate, like a pin cushion or prolate,like a cigar). This moment can be expressed by the integral of nuclear volume $d\tau$:

$$eQ_o = \int (3\zeta^2 - r^2)\rho(r)d\tau \quad , \tag{4.9}$$

where r is the distance from the center of the charge distribution and ζ is the coordinate in the direction of the rotationally symmetric axis. Because the electrons in

the system produce an inhomogeneous but rotaionally symmetric electric field, the interaction of this field and the charge distribution results in a shift in the energy levels:

$$\Delta H_Q = \frac{1}{4} eQ_o \frac{\partial^2 V}{\partial z^2} (\frac{3}{2}\cos^2(\theta) - \frac{1}{2}) \quad , \tag{4.10}$$

where θ is the angle between the symmetry axis of the nuclear charge distribution and the symmetry axis of the electronic motion.

In the case of a free atom the rotationally symmetric axis of the quadrupole moment and the total nuclear angular momentum, $\vec{I}$, are colinear. The axis of rotational symmetry of the electric potential created by the electron is, in turn, colinear with the total electronic angular momentum, $\vec{J}$. In general, $\vec{I}$ and $\vec{J}$ are not colinear, but are at some fixed angle with respect to one another. This causes them to precess. Due to this precession of the nucleus, the interaction energy involves the time-average of the quadrupole moment. Quantum mechanically we write (Kopfermann 1958), (Woodgate 1983):

$$Q = Q_o \frac{I(2I+1)}{(J+1)(2J+1)} \quad . \tag{4.11}$$

where the nuclear charge distribution is prolate if $Q > 0$ and oblate for $Q < 0$ and the magnitude is determined by the time-average of r^2.

We can express the resultant perturbation from 4.10 using quantum mechanical operators of the total angular momenta (with θ as given by the cosine mentioned in the magnetic dipole interaction):

$$\Delta H_Q = eQ \frac{\partial^2 V}{\partial z^2} \frac{[3(\vec{I}\cdot\vec{J})^2 + \frac{3}{2}(\vec{I}\cdot\vec{J}) - I(I+1)J(J+1)]}{2I(2I-1)J(2J-1)} \quad . \tag{4.12}$$

Where we can extract $B = eQ\frac{\partial^2 V}{\partial z^2}$ from experimental measurements of $\frac{1}{\hbar}(\Delta E_{Q_e} - \Delta E_{Q_g})$ between the ground and excited states. The first-order energy shift due to the

quadrupole interaction can finally be written in terms of the total angular momentum of the atom:

$$\Delta E_Q = \frac{B}{4}\frac{\frac{3}{2}K(K+1) - 2I(I+1)J(J+1)]}{2I(2I-1)J(2J-1)} \quad , \tag{4.13}$$

where $K = F(F+1) - I(I+1) - J(J+1)$.

When an external magnetic field $\vec{B}_{ex}$ is applied along the $z-$axis in the presence of the atom, it interacts with the total electronic magnetic moment, $\vec{\mu}_J$, and nuclear magnetic moment, $\vec{\mu}_I$. This interaction is the called the Zeeman effect. In the limit of weak fields I and J are still stongly coupled. In the strong field limit I and J are coupled more strongly to the external magnetic field than to each other. If we assume interactions that are internal to the electronic system are excluded from the perturbation (i.e. they reside within the H_o, the zeroth order Hamiltonian), we can write this perturbation as:

$$\begin{aligned} \Delta H_Z &= -\vec{\mu}_I \cdot \vec{B}_{ex} - \vec{\mu}_J \cdot \vec{B}_{ex} \\ &= -g_I \mu_B I_z B_{ex} + g_J \mu_B J_z B_{ex} \end{aligned} \tag{4.14}$$

Now we are able to write the entire perturbation Hamiltonian:

$$\begin{aligned} \Delta H &= \Delta H_D + \Delta H_Q + \Delta H_Z \\ &= A(\vec{I}\cdot\vec{J}) + B\frac{[3(\vec{I}\cdot\vec{J})^2 + \frac{3}{2}(\vec{I}\cdot\vec{J}) - I(I+1)J(J+1)]}{2I(2I-1)J(2J-1)} \\ &- \vec{\mu}_I \cdot \vec{B}_{ex} - \vec{\mu}_J \cdot \vec{B}_{ex}. \end{aligned} \tag{4.15}$$

4.2 The Hyperfine Structure of Magnesium

^{24}Mg has a total nuclear angular momentum of $I = 0$. This leads to energy levels that are not split by hyperfine interactions. ^{25}Mg, on the other hand, has

one additional nucleon in its nucleus compared with ^{24}Mg. Although this does not increase the electronic or nuclear charge of the atom, it does alter the nuclear angular momentum. Also, due to the addition of a spatially finite particle, a neutron, the distribution of protons (and, therefore, charge) is altered, giving rise to the magnetic dipole and electric quadrupole interactions.

This isotope has a total nuclear angular momentum $I = \frac{5}{2}$ with associated nuclear magnetic quantum number m_I with values $I, I-1, ..., -I$. The total electronic angular momentum is J and its associated quantum number has values, $m_J = J, J-1, ..., -J$. Together, these quantities make up the total atomic angular momentum $F = I + J$, and it follows that the corresponding quantum number, $m_F = I+J, I+J-1, ..., |I-J|$.

The energy levels that we are concerned with are the $1s^2 2s^2 2p^6 3s\ ^2S_{\frac{1}{2}}$, $1s^2 2s^2 2p^6 3s\ ^2P_{\frac{1}{2}}$ and $1s^2 2s^2 2p^6 3s\ ^2P_{\frac{3}{2}}$. The first two levels, $^2S_{\frac{1}{2}}$ and $^2P_{\frac{1}{2}}$, have a maximum total angular momentum of $F = 3$, which gives rise to their level being split into three (by hyperfine splitting) and each of these sublevels are split into $2F + 1$ by the Zeeman interaction. These two levels are only affected by the magnetic dipole interaction since the electronic charge distribution is spherically symmetric for $J = \frac{1}{2}$, according to the assumptions made previously.

The $^2P_{\frac{3}{2}}$ level has a maximum total angular momentum of $F = 4$. The hyperfine structure splits the level into four, and these levels are split into $2F + 1$ levels by the Zeeman interaction. This level is the only one under consideration that is affected by both the magnetic dipole and the electric quadrupole moments of the atom.

The constants for the magnetic dipole and electric quadrupole interaction, that are specific to the energy level of the atom in question, are determined by measuring the frequency of light that is emitted from a certain transition. The ground state constant in the magnetic dipole interation was determined experimentally (Itano and Wineland

1981) to be $a_{S_{\frac{1}{2}}} = \frac{1}{\hbar}A_{S_{\frac{1}{2}}} = -596.254376(54)$MHz. The other constants, using atomic structure calculations (Itano 2004) (using GRASP92 programs (Parpia, Fischer, and Grant 1996) to get Dirac-Hartree-Fock wavefunctions and HFS92 (Jonsson, Parpia, and Fischer 1996) in order to calculate the hyperfine constants), were determined to be: $a_{P_{\frac{1}{2}}} = \frac{1}{\hbar}A_{P_{\frac{1}{2}}} = -100.1649$MHz and $a_{P_{\frac{3}{2}}} = \frac{1}{\hbar}A_{P_{\frac{3}{2}}} = -19.0972$MHz. Also calcuated was the electric quadrupole interaction constant: $b_{P_{\frac{3}{2}}} = \frac{1}{\hbar}B_{P_{\frac{3}{2}}} = +22.3413$MHz.

4.3 Hyperfine Calculation

Since the hyperfine structure of the excited states will be an important part of future experiments in our lab, the shifts due to hyperfine interactions are calculated. The equation used in the calculation of the hyperfine structure of $^{25}Mg^{+}$, as mentioned above, is the exact solution to the shift in energy levels due to the magnetic dipole and electric quadrupole contribuitons to the hyperfine splitting as well as the Zeeman shift due to an external magnetic field. The $^2S_{\frac{1}{2}}$ and $^2P_{\frac{1}{2}}$, or $J = \frac{1}{2}$, levels have symmetric charge distributions and therefore there is no electric quadrupole contribution for these states. The calculations were done in terms of frequencies:

$$\begin{aligned}\frac{1}{\hbar}(\Delta H &= \Delta H_D + \Delta H_Q + \Delta H_Z) \\ &= \frac{1}{\hbar}[A(\vec{I}\cdot\vec{J}) + B\frac{[3(\vec{I}\cdot\vec{J})^2 + \frac{3}{2}(\vec{I}\cdot\vec{J}) - I(I+1)J(J+1)]}{2I(2I-1)J(2J-1)} \\ &- \vec{\mu}_I\cdot\vec{B}_{ex} - \vec{\mu}_J\cdot\vec{B}_{ex}]. \end{aligned} \tag{4.16}$$

Where the above operators are defined in the usual way (Griffiths 1995): $\vec{X} = X_x\hat{i} + X_y\hat{j} + X_z\hat{k}$ where $\vec{X} = \vec{I}, \vec{J}$. The $|m_I, m_J\rangle$ basis was used, leaving the matrix in the form $\langle m_I, m_J|\Delta H|m_I, m_J\rangle$; this notation made the organization of the matrix elements more transparent than when looking at the $|F, m_F\rangle$ basis. There are 24 terms, $(2I+1)(2J+1)$, which translates to a 12×12 matrix for the $^2S_{\frac{1}{2}}$ and $^2P_{\frac{1}{2}}$

states and a 24×24 matrix for the $^2P_{\frac{3}{2}}$. Obviously, it is desirable to find a way to increase the efficiency of the diagonalization of the matrices in this calculation. It was found, using the $|m_I, m_J\rangle$ basis, that we could organize the matrix into a block diagonal matrix, with the largest block being 4×4 for $^2P_{\frac{3}{2}}$ and 2×2 for the $^2S_{\frac{1}{2}}$ and $^2P_{\frac{1}{2}}$ states. The $^2S_{\frac{1}{2}}$ and $^2P_{\frac{1}{2}}$ were diagonalized using Maple and Matlab; this was done analytically and was done with computational ease since the matrices were fairly simple due to the absence of the electric quadrupole term (from symmetry arguments). An example of one of the 2×2 block diagonal matrix of the $^2P_{\frac{1}{2}}$ level is as follows for $m_I = \frac{5}{2}$, $m_J = \frac{-1}{2}$ and $m_I = \frac{3}{2}$, $m_J = \frac{1}{2}$ corresponding to $m_F = 2$:

$$\begin{bmatrix} \frac{-5}{4}A + \frac{-5}{2}H_I + \frac{1}{2}H_J & \sqrt{5}\frac{A}{2} \\ \sqrt{5}\frac{A}{2} & \frac{3}{4}A + \frac{-3}{2}H_I + \frac{-1}{2}H_J \end{bmatrix}$$

where $H_I = g_I' \mu_B B_{ex}$; $H_J = -g_J \mu_B B_{ex}$; g_I' and g_J are the nuclear and electronic g-factors. A plot of the energy level splitting with respect to magnetic field is shown in Figure 4.1 for the $^2S_{\frac{1}{2}}$ level and Figure 4.2 for the $^2P_{\frac{1}{2}}$ level.

The matrix for the hyperfine splitting of the $^2P_{\frac{3}{2}}$ state was diagonalized successfully using Matlab; due to the quadrupole shifts in the $^2P_{\frac{3}{2}}$ state the matrix has more terms and is more difficult to diagonalize than the $^2S_{\frac{1}{2}}$ and $^2P_{\frac{1}{2}}$ states that do not have electric quadrupole contributions. As an example of one of the block matrices for the $F = 0$ $^2P_{\frac{3}{2}}$ states $|m_I = \frac{3}{2}, m_J = \frac{-3}{2}\rangle$, $|m_I = \frac{1}{2}, m_J = \frac{-1}{2}\rangle$, $|m_I = \frac{-1}{2}, m_J = \frac{1}{2}\rangle$, $|m_I = \frac{-3}{2}, m_J = \frac{3}{2}\rangle$ is :

$$\begin{bmatrix} \frac{-9}{4}A + \frac{-3}{2}H_I + \frac{3}{2}H_J + \frac{-1}{20}B & \sqrt{6}A + \frac{-\sqrt{1}}{10}B & \frac{3\sqrt{6}}{20}B & 0 \\ \sqrt{6}A + \frac{-\sqrt{6}}{10}B & \frac{-1}{4}A - \frac{1}{2}H_I + \frac{1}{2}H_J + \frac{1}{5}B & 3A & \frac{3\sqrt{6}}{20}B \\ \frac{3\sqrt{6}}{20}B & 3A & \frac{-1}{4}A - \frac{1}{2}H_I + \frac{1}{2}H_J + \frac{1}{5}B & \sqrt{6}A + \frac{-\sqrt{6}}{10}B \\ 0 & \frac{3\sqrt{6}}{20}B & \sqrt{6}A + \frac{-\sqrt{6}}{10}B & \frac{-9}{4}A + \frac{3}{2}H_I + \frac{-3}{2}H_J + \frac{-1}{20}B \end{bmatrix}$$

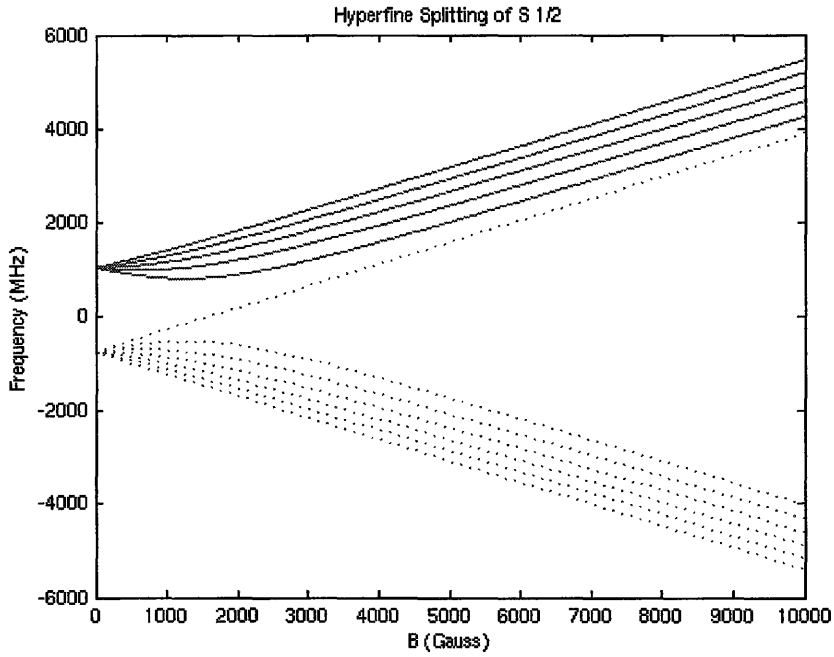

Figure 4.1: Plot of the energy level splitting as a function of magnetic field (B in Gauss) in the $^2S_{\frac{1}{2}}$ level due to hyperfine and Zeeman shifts. Plotted in Matlab.

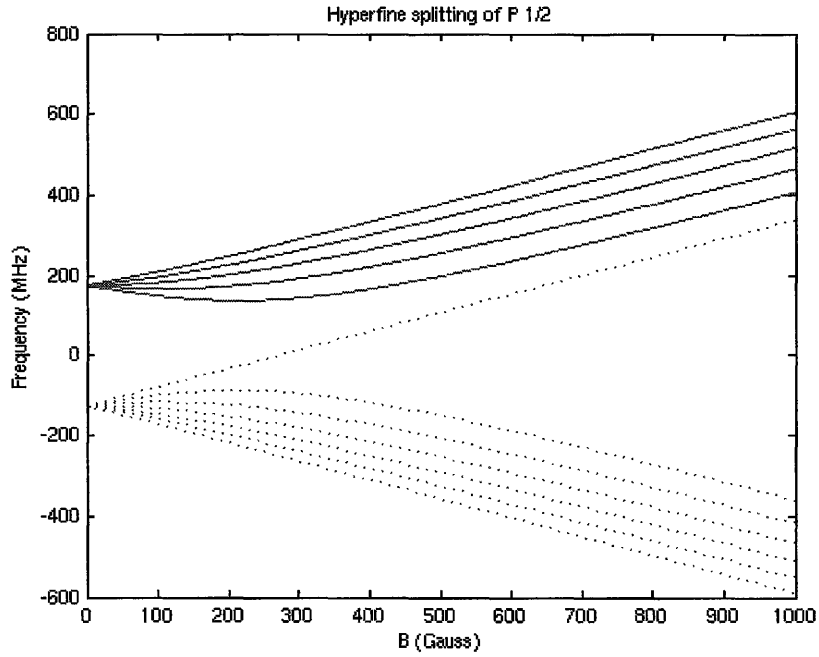

Figure 4.2: Plot of the energy level splitting as a function of magnetic field (B in Gauss) in the $^2P_{\frac{1}{2}}$ level due to hyperfine and Zeeman shifts. Plotted in Matlab.

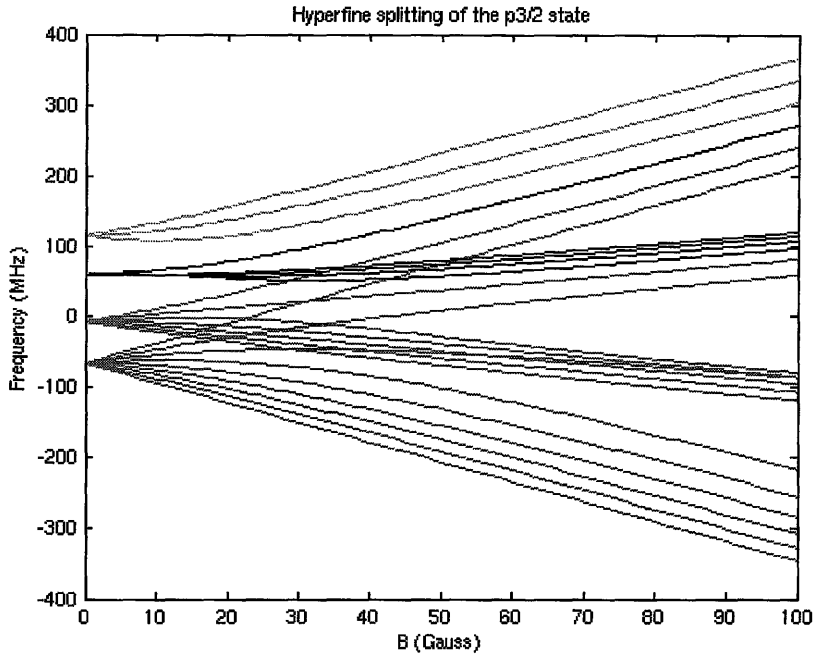

Figure 4.3: Plot of the energy level splitting as a function of magnetic field (B in Gauss) in the $^2P_{\frac{3}{2}}$ level due to hyperfine and Zeeman shifts. Plotted in Matlab.

Attempts to diagonalize the matrices of this size using Maple failed to converge in a reasonable amount of time, so the problem was redone using Matlab. The code for all three states can be seen in Appendix A.

The results of the calculations for the $^2P_{\frac{3}{2}}$ are shown in Figure 4.3 these figures have a large enough range in magnetic field to see the two limiting cases: weak and strong external magnetic fields. These are also referred to as the Zeeman and Paschen-Back regimes, respectively. In the case of the application of a weak magnetic field to the atom, the splitting of the hyperfine levels is approximately linear where each hyperfine level is split into $2F+1$ separate components. The angular momenta, I and J are strongly coupled and the hyperfine splitting is approximately

$$\Delta H_{WF} = g_F \mu_B m_F B_{ex} \ , \tag{4.17}$$

where $g_F = g_J \frac{F(F+1)+J(J+1)-I(I+1)}{2F(F+1)} - g'_I \frac{F(F+1)-J(J+1)+I(I+1)}{2F(F+1)}$ and $m_f = m_I + m_J$. In the Paschen-Bach regime, the hyperfine levels are redistributed into $2J+1$ groups and are split evenly into $2I+1$ sublevels that vary linearly with magnetic field. The effect of the strong electronic moment and the relatively weak nuclear moment is that their angular momenta are no longer coupled, so that F is no longer a well-defined quantum number. In this strong-field limit we can write the hyperfine splitting as

$$\Delta H_{SF} = g_J \mu_B m_J B_{ex} + A m_I m_J - g'_I \mu_B m_I B_{ex} \quad . \tag{4.18}$$

As a method for double checking the exact calculation, we can use these limits to confirm that the calculations are correct. Both weak and strong field limits agree with the calculation.

Chapter 5

Linewidth Measurement of ^{24}Mg

Spectroscopic measurements on single particles have many advantages over spectroscopic measurements taken with large numbers of atoms, like an atomic beam or a contained gas. When we observe a single ion, there is no broadening of its spectrum due to collisions and the spectral information does not need to be treated as due to a distribution of particles. Also, due to the ability to cool the ion, we can make the effects of Doppler broadening negligible. The following chapter will discuss proposed measurements of the linewidths of the $^2S_{\frac{1}{2}} \longrightarrow ^2 P_{\frac{3}{2}}$ trasition of ^{24}Mg. The experimental set-up will be outlined as well as possible broadening mechanisms and how they are characterized.

5.1 Linewidth in ^{24}Mg

In our lab, the first experiment/measurement to be done with magnesium will be a precise determination of the linewidth of the ^{24}Mg ion. Due to the absence of nuclear angular momentum in elemental ^{24}Mg, there is no hyperfine spitting of its levels. This makes the measurement straightforward in that we don't have to worry about the overlap of multiple hyperfine sublevels. This linewidth measurement will allow us to gather information about $^{24}Mg^+$ and $^{25}Mg^+$ since the lifetime, set by the spontaneous emission rate, will be approximately the same for both ions. The lifetimes of each isotope will differ slightly from each other due to a small isotope shift of the energy levels of ^{25}Mg.

It is known that the linewidth, Γ, of $^{24}Mg^{+}$ is about 45MHz (Nagourney, Janik, and Dehmelt 1983). We propose to perform a linewidth measurement that is more precise that the current figure. Due to the narrow linewidth of our fiber laser, we are able to resolve the spectrum to a higher degree (our laser linewidth of 174kHz as opposed to their $<$ 1MHz laser linewidth). The purpose of the measurement is to obtain the highest precision measurement of the linewidth of $^{24}Mg^{+}$; this is useful in other fields such as observational astrophysics and atomic structure theory.

In order to carry out this experiment we start off by optically pumping our trapped ion into the state of greatest angular momentum, $|F = \frac{3}{2}, m_F = \frac{3}{2}\rangle$ of the $^2S_{\frac{1}{2}}$ state with a strong laser beam of σ^+ polarized light. This prepares the ion in a state so that it can be cooled with the cycling transition (used for cooling and detection) which allows for a large number of scattering events because there is only one state for the ion to excite or decay into. If we now take a weak laser beam and scan over the resonance , ω_o, of the transition with a scan width of at least a few linewidths we are able to trace out the entire Lorentzian intensity distribution as a function of frequency. The reason for using a weak probe beam is due to the effect of power broadening. By taking multiple profiles with different beam powers we are able to extract the amount of broadening of the linewidth since we know the relationsip between the intensity of the beam and the amount the by which the intensity profile will be smeared (see Section 2.2).

We obtain the intensity spectrum by collecting the fluorescence that is emitted from the ion for each detuning $\delta\omega$ over the scanning range, and plotting this intensity distribution as a function of the frequency of the laser beam. We then use mathematical software to fit the plot to a Lorentzian curve; since we know the relationship between the linewidth and the Lorentzian function, the line width can be extracted.

The outline of a typical experiment is as follows: we will need to optically pump, Doppler cool and use the cycling transition to probe the ion. The optical pumping and Doppler cooling beams are essentially the same; a strong beam of σ^+ polarized light is incident on the ion and once the ion is optically pumped into the cycling transition, the laser frequency, detuned on the order of 100MHz, is scanned – increasing the frequency toward resonance in order to facilitate cooling. These lasers are left on for about $10\mu s$ in order to completelly cool and prepare the ion. A π pulse of 2.18ns, which is characteristic of $^{24}Mg^+$, is then carried out with the weaker probe beam and the fluorescence is collected by the photomultiplier tube PMT. This procedure is repeated at the same frequency 1000 times, repeated for a range of greater than 2Γ over approximately 1000 different frequencies.

The π pulse allows us to excite from the ground state $^2S_{\frac{1}{2}}$ level $|J=\frac{1}{2}, m_J=\frac{1}{2}\rangle$to the $^2P_{\frac{1}{2}}$ level $|J=\frac{1}{2}, m_J=\frac{1}{2}\rangle$ with the highest probability of ending up in the excited state.

5.2 Previous Measurements

The natural linewidth of $^{24}Mg^+$ has been measured by W.Nagourney, G.Janik and H.Dehmelt and was found to be $\Gamma=2\pi$ 45.67(5.9)MHz. The experiment was published in January 1983 (see (Nagourney, Janik, and Dehmelt 1983)). The ion was trapped in an rf trap, cooled to approximately 5mK and probed with laser powers of less than 22μW. Photon counting was accomplished with a photomultiplier tube and the overall collection efficiency on the order of .001%. The uncertainty in the measurement is 5.9 MHz which they claim is due mainly to the drift of the laser frequency (which was <1MHz/min). Other limits that were face by the team were residual gas heating and a laser linewidth of 1.5MHz.

Some of our apparatus specifications (Doppler cooling limit, laser linewidth and drift rate) are now estimated. Since we are in the weak binding regime for Doppler cooling, we will use the Doppler limit for a free atom (Wineland and Itano 1979):

$$\begin{aligned} \langle E_k \rangle_{min} &= \frac{1}{4}\hbar\Gamma \\ &= \frac{1}{2}k_b T \\ T_{min} &= \frac{\hbar}{2k_B}2\pi \cdot 43MHz, \end{aligned} \tag{5.1}$$

the resulting minimum temperature is 1.03mK. The linewidth of our fiber lasers is 174kHz and their drift rate is less than 1MHz/min.

Chapter 6

Conclusion

Ions confined to a small region in space by electric fields are virtually free from perturbations, have well-characterized motion and are sensitive to specific UV wavelengths. These properties make a single ion (or a small group of ions) easy to manipulate. The ion's ability to emit large numbers of photons also allows measurement of its state of the ion. For these reasons, ions in electromagnetic traps offer many advantages in making precise measurements and probing quantum mechanical properties. $^{25}Mg^{+}$ can be used to realized a two-level sytem, whichenables experiments in quantum information and quantum behaviour.

In our lab, we have three laser systems. The dye laser can be used for photo-ionization due to its high power. Since the dye laser has a large linewidth, it cannot be used for ion manipulation but is suitable for Doppler cooling. The 2W fiber laser was to be used for driving Doppler cooling on the cycling transition of the ion. Because of its narrow linewidth this laser is ideal for making precise spectroscopic measurements. The 1W fiber laser was set up with the intention of using it to excite the $^{2}P_{\frac{1}{2}}$ transition in Mg^{+}. Currently, the 2W fiber laser is broken and the functions that were once to be performed by this laser have had to be redistributed. The sole purpose of the dye laser at this time is to drive the cycling transition. Photo-ionization has now been replaced with electron impact ionization using the electron guns inside the vacuum chamber. The 1W fiber laser, however, is still intended to drive the $^{2}P_{\frac{1}{2}}$ transition.

A Doppler-free saturated iodine spectrum has been taken that maps the hyperfine transtions in an iodine transition that is in the frequency range of the $^2P_{\frac{1}{2}}$ transition. This spectrum was taken with the 1W fiber laser and is valuable because it gives us a way to stably lock our laser to an iodine feature that is only on the order of 100MHz away from the Mg^+ transition.

Hyperfine calculations were done and provide an exact solution to the splitting of energy levels with respect to the applied magnetic field. With these calculations we are now able calculate how our system behaves, which will be useful for experiments. Knowing the theoretical hyperfine splitting of our ion will also allow us to find the value of magnetic field that will allow us to spectroscopically resolve the hyperfine levels, possibly allowing us to measure the $^2P_{\frac{1}{2}}$ and $^2P_{\frac{3}{2}}$ hyperfine structure and constants. These measured values can be used by others as a way to compare values in atomic structure codes.

Currently, our apparatus includes an operational dye laser (~600 mW @ 560nm), which stably locks. The dye laser's beam is then sent into the fully operational Wavetrain frequency doubling cavity (producing 1-2 mW @ 280nm). The 1W fiber laser is stably locked to iodine and generates about 2.5mW in the UV. When the 2W fiber laser was operational it typically generated 1.1mW of UV power. The vacuum chamber is kept at 5.5×10^{-11}torr, the magnesium ovens are vaporizing non-negligible amounts of magnesium and the electron guns are producing a measureable flux of electrons. We are currently attempting to trap ions and hope to trap ions in the near future.

Once we trap ions, we will make a measurement of the linewidth of Mg^+. We intend to follow this experiment with a measurement of the hyperfine coefficients of $^{25}Mg^+$. Our group will go on to invesigate quantum computation algorithms and study more general quantum behaviour.

Appendix A

Hyperfine Calculation Code

The code that follows is the actual code used in finding the hyperfine splitting and the Zeeman shifts for $^{25}Mg^{+}$ using Matlab.

6.1 Matlab Code for the $^2S_{\frac{1}{2}}$ State Energy Level Splitting

```
 close all
clear all


%syms B
%gi gj
%lambda


B=[0:1:10000];


ii=1;
for ii=1:length(B)
    clear MD
    clear MA
    clear MB
```

```
    clear MC
    clear ME
    clear MF
    clear MG
    clear MH
    clear MI

    ii;

    muB=1.4;
    lambda=0;
    aa=(-596.254376);
    H=muB*B(ii);
    gi=0.8554*(1.4/1836.13);
    gjj=-(4-2.002319304)/3;
    hi=gi*H;
    hjj=gjj*H;

A1=(aa*5/4 -5/2 *hi -1/2 *hjj) ;
MA = [A1];

B11=(-aa*5/4 -5/2 *hi +1/2 *hjj) ;
B12=aa*sqrt(5)/2 ;
B21=aa*sqrt(5)/2;
B22=(3/4*aa - 3/2 *hi - 1/2 *hjj) ;
MB = [B11 B12 ; B21 B22];
```

```
C11=(-aa*3/4 -3/2 *hi +1/2 *hjj) ;

C12=aa*sqrt(8)/2 ;

C21=aa*sqrt(8)/2 ;

C22=(1/4*aa - 1/2 *hi - 1/2 *hjj) ;

MC = [C11 C12 ; C21 C22];


D11=(-aa*1/4 -1/2 *hi +1/2 *hjj) ;

D12=aa*3/2 ;

D21=aa*3/2 ;

D22=(-1/4*aa +1/2 *hi - 1/2 *hjj) ;

MD = [D11 D12 ; D21 D22];


E11=(aa*1/4 +1/2 *hi +1/2 *hjj) ;

E12=aa*sqrt(8)/2 ;

E21=aa*sqrt(8)/2 ;

E22=(-3/4*aa +3/2 *hi - 1/2 *hjj) ;

ME = [E11 E12 ; E21 E22];


F11=(3/4*aa +3*hi/2 + hjj/2) ;

F12=aa*sqrt(5)/2 ;

F21=aa*sqrt(5)/2 ;

F22=(-5/4 *aa + 5*hi/2 - hjj/2) ;

MF = [F11 F12; F21 F22];


    G11=((5/4)*aa + 5*hi/2 + 1*hjj/2) ;
```

```
MG = [G11];



     AA=eig(MA);
    eig1a(ii)=AA(1);


    BB=eig(MB);
    eig1b(ii)=BB(1);
    eig2b(ii)=BB(2);

CC=eig(MC);
    eig1c(ii)=CC(1);
    eig2c(ii)=CC(2);

DD=eig(MD);
    eig1d(ii)=DD(1);
    eig2d(ii)=DD(2);

EE=eig(ME);
    eig1e(ii)=EE(1);
    eig2e(ii)=EE(2);

     FF=eig(MF);
    eig1f(ii)=FF(1);
    eig2f(ii)=FF(2);
```

```
     GG=eig(MG);
    eig1g(ii)=GG(1);


    ii=ii+1;
end


figure


plot(B,eig1a,'b:',...
    B,eig1b,'b:',B,eig2b,'r',...
B,eig1c,'b:',B,eig2c,'r',...
B,eig1d,'b:',B,eig2d,'r',...
B,eig1e,'b:',B,eig2e,'r',...
    B,eig1f,'b:',B,eig2f,'r',...
    B,eig1g,'b:')


%legend('1','2','3','4','5','6')
```

6.2 Matlab Code for the $^2P_{\frac{1}{2}}$ State Energy Level Splitting

```
 close all
clear all


%syms B
%gi gj
```

```
%lambda


B=[0:1:1000];


ii=1;
for ii=1:length(B)
    clear MD
    clear MA
    clear MB
    clear MC
    clear ME
    clear MF
    clear MG
    clear MH
    clear MI


    ii;


    muB=1.4;
    lambda=0;
    aa=(-100.1649);
    H=muB*B(ii);
    gi=0.8554*(1.4/1836.13);
    gjj=-(4-2.002319304)/3;
    hi=gi*H;
    hjj=gjj*H;
```

```
A1=(aa*5/4 -5/2 *hi -1/2 *hjj) ;
MA = [A1];

B11=(-aa*5/4 -5/2 *hi +1/2 *hjj) ;
B12=aa*sqrt(5)/2 ;
B21=aa*sqrt(5)/2;
B22=(3/4*aa - 3/2 *hi - 1/2 *hjj) ;
MB = [B11 B12 ; B21 B22];

C11=(-aa*3/4 -3/2 *hi +1/2 *hjj) ;
C12=aa*sqrt(8)/2 ;
C21=aa*sqrt(8)/2 ;
C22=(1/4*aa - 1/2 *hi - 1/2 *hjj) ;
MC = [C11 C12 ; C21 C22];

D11=(-aa*1/4 -1/2 *hi +1/2 *hjj) ;
D12=aa*3/2 ;
D21=aa*3/2 ;
D22=(-1/4*aa +1/2 *hi - 1/2 *hjj) ;
MD = [D11 D12 ; D21 D22];

E11=(aa*1/4 +1/2 *hi +1/2 *hjj) ;
E12=aa*sqrt(8)/2 ;
E21=aa*sqrt(8)/2 ;
E22=(-3/4*aa +3/2 *hi - 1/2 *hjj) ;
```

```
ME = [E11 E12 ; E21 E22];


F11=(3/4*aa +3*hi/2 + hjj/2) ;
F12=aa*sqrt(5)/2 ;
F21=aa*sqrt(5)/2 ;
F22=(-5/4 *aa + 5*hi/2 - hjj/2) ;
MF = [F11 F12; F21 F22];


    G11=((5/4)*aa + 5*hi/2 + 1*hjj/2) ;
MG = [G11];



     AA=eig(MA);
    eig1a(ii)=AA(1);


    BB=eig(MB);
    eig1b(ii)=BB(1);
    eig2b(ii)=BB(2);


CC=eig(MC);
    eig1c(ii)=CC(1);
    eig2c(ii)=CC(2);


DD=eig(MD);
    eig1d(ii)=DD(1);
    eig2d(ii)=DD(2);
```

```
EE=eig(ME);
    eig1e(ii)=EE(1);
    eig2e(ii)=EE(2);

     FF=eig(MF);
    eig1f(ii)=FF(1);
    eig2f(ii)=FF(2);

     GG=eig(MG);
    eig1g(ii)=GG(1);

    ii=ii+1;
end

figure

plot(B,eig1a,'b:',...
    B,eig1b,'b:',B,eig2b,'r',...
B,eig1c,'b:',B,eig2c,'r',...
B,eig1d,'b:',B,eig2d,'r',...
B,eig1e,'b:',B,eig2e,'r',...
    B,eig1f,'b:',B,eig2f,'r',...
    B,eig1g,'b:')

%legend('1','2','3','4','5','6')
```

6.3 Matlab Code for the $^2P_{\frac{3}{2}}$ State Energy Level Splitting

```
 close all
clear all


%syms B
%gi gj
%lambda


B=[0:1:100];


ii=1;
for ii=1:length(B)
    clear MD
    clear MA
    clear MB
    clear MC
    clear ME
    clear MF
    clear MG
    clear MH
    clear MI


    ii;


    muB=1.4;
```

```
    lambda=0;
     b=22.3413/(60);
% b=0;
    a=(-19.0972);
    H=muB*B(ii);
    gi=0.8554*(1.4/1836.13);
    gj=-(2+2.002319304)/3;
    q=525/16;
    hi=gi*H;
    hj=gj*H;
    bb=22.3413;

A1=(a*15/4 -5/2 *hi -3/2 *hj) + b*(3*(25*9/16) + 3/2 *15/4 -q);
MA = [A1];

B11=(a*5/4 -5/2 *hi -1/2 *hj) + b*(3*(25/16 +15/4) + 3/2* 5/4 -q);
B12=a*sqrt(15)/2 + b*(3/2 *(14/4 *sqrt(15)) + 3/2 *sqrt(15)/2);
B21=a*sqrt(15)/2 + b*(3/2 *(14/4 *sqrt(15)) + 3/2 *sqrt(15)/2);
B22=(9/4*a - 3/2 *hi - 3/2 *hj) + b*(3*(81/16+15/4) + 3/2 *9/4 -q);
MB = [B11 B12 ; B21 B22];

C11=(-5*a/4 - 5/2*hi +1/2*hj) + b*(3*(25/16+5) +3/2 *(-5)/4 - q);
C12=a*sqrt(5);
C13=b*3*sqrt(30);
C21=a*sqrt(5);
C22=(a*3/4 -3/2 *hi - 1/2* hj) + b*(3*(9/16 + 11) + 3/2*3/4 -q);
```

```
C23=a*sqrt(6) + b*(3/2 *(3*sqrt(6)) + 3/2 *sqrt(6));

C31=b*3*sqrt(30);

C32=a*sqrt(6) + b*(3/2 *(3*sqrt(6)) +3/2 *sqrt(6));

C33=(a*3/4 -1/2 *hi -3/2 *hj) + b*(3*(9/16 + 6) + 3/2 *(3/4) - q);

MC = [C11 C12 C13 ; C21 C22 C23; C31 C32 C33];


D11=(-15)*a/4 - 5/2 *hi +3/2*hj + b*(3*(25*9/16 +15/4) + 3/2 *(-15/4)-q);

D22=(-3)*a/4 - 3/2 *hi + 1/2 *hj +b*(3*(9/16 + 47/4) + 3/2*(-3/4) - q);

D33=(a/4 -1/2 *hi -1/2 *hj) + b*(3*(1/16 + 59/4) + 3/8 - q);

D44=(-3)*a/4 + 1/2 *hi -3/2 *hj + b*(3*(9/16 + 27/4) + 3/2*(-3/4) - q);

D12=a/2 *sqrt(15) + b*(3/2 *(-18/4*sqrt(15)) + 3/2 *sqrt(15)/2);

D13=b*3*sqrt(30);

D14=0;

D21=a/2*sqrt(15) + b*(3/2*(-18/4*sqrt(15)) + 3/2 *sqrt(15)/2);

D23=a*sqrt(8);

D24=b*9*sqrt(6);

D31=b*3*sqrt(30);

D32=a*sqrt(8) ;

D34=(3*a/2)*sqrt(3);

D41=0;

D42=b*9*sqrt(6);

D43=(3*a/2)*sqrt(3);

MD=[D11 D12 D13 D14; D21 D22 D23 D24 ;D31 D32 D33 D34; D41 D42 D43 D44];


E11=(-9)*a/4 -3/2 *hi + 3/2 *hj + b*(3*(81/16+ 6) +3/2*(-9/4) - q);

E22=(-1)*a/4 -1/2*hi+1/2*hj + b*(3*(1/16+15) + 3/2*(-1/4) - q);
```

```
E33=(-1)*a/4 +1/2*hi-1/2*hj + b*(3*(1/16 +15) + 3/2*(-1/4) -q);

E44=(-9)*a/4 +3/2*hi -3/2*hj + b*(3*(81/16 +6) +3/2*(-9/4) -q);

E12=a*sqrt(6) + b*(3/2*(-4)*sqrt(6));

E13=b*9*sqrt(6);

E14=0;

E21=a*sqrt(6) + b*(3/2*(-4)*sqrt(6));

E23=(a)*3;

E24=b*9*sqrt(6);

E31=b*9*sqrt(6);

E32=(a*3);

E34=a*sqrt(6) + b*(3/2*(-4)*sqrt(6));

E41=0;

E42=b*9*sqrt(6);

E43=a*sqrt(6)+ b*(3/2*(-4)*sqrt(6));

ME=[E11 E12 E13 E14;E21 E22 E23 E24;E31 E32 E33 E34; E41 E42 E43 E44];


F11=(-3)*a/4 -1/2*hi +3/2*hj + b*(3*(9/16 +27/4) + 3/2 *(-3/4)- q);

F22=a/4+ +1/2*hi +1/2*hj + b*(3*(1/16 +59/4) +3/2/4 -q);

F33=(-3)*a/4+3/2*hi -1/2*hj + b*(3*(9/16 +47/4) + 3/2*(-3/4) -q);

F44=(-15)*a/4+5/2*hi-3/2*hj + b*(3*(9*25/16 +15/4) + 3/2*(-15/4) -q);

F12=(3*a/2)*sqrt(3);

F13=b*9*sqrt(6);

F14=0;

F21=(a*3/2)*sqrt(3);

F23=(a)*sqrt(8);

F24=b*3*sqrt(30);
```

```
F31=b*9*sqrt(6);

F32=(a)*sqrt(8);

F34=(a/2)*sqrt(15) + b*(3/2*(-18/4)*sqrt(15) + 3/2*sqrt(15)/2);

F41=0;

F42=b*3*sqrt(30);

F43=(a/2)*sqrt(15)+ b*(3/2*(-18/4)*sqrt(15) + 3/2*sqrt(15)/2);

MF=[F11 F12 F13 F14;F21 F22 F23 F24;F31 F32 F33 F34;F41 F42 F43 F44];


G11=(a*3/4 +hi/2 + 3*hj/2) + b*(3*(9/16 +6) + 3/2*3/4 -q);

G12=a*sqrt(6) + b*(3/2*(3*sqrt(6)) + 3/2*sqrt(6));

G13=b*3*sqrt(30);

G21=a*sqrt(6) + b *(3/2*3*sqrt(6) +3/2*sqrt(6));

G22=(a*3/4 + 3*hi/2 + hj/2) + b*(3*(9/16 + 11) + 3/2*3/4 - q);

G23=a*sqrt(5);

G31=b*3*sqrt(30);

G32=a*sqrt(5);

G33=(-5/4 *a + 5/2 *hi - hj/2) + b*(3*(25/16 + 5) + 3/2 *(-5/4) -q);

MG = [G11 G12 G13; G21 G22 G23; G31 G32 G33];


H11=(9/4*a +3*hi/2 + 3*hj/2) + b*(3*(81/16 +15/4)+3/2*9/4 -q);

H12=a/2*sqrt(15) + b*(3/2*(5*sqrt(15)/4 + 9*sqrt(15)/4)+ 3/2*sqrt(15)/2);

H21=a/2*sqrt(15) + b*(3/2*(5*sqrt(15)/4 + 9*sqrt(15)/4)+ 3/2*sqrt(15)/2);

H22=(5/4 *a + 5*hi/2 + hj/2) + b*(3*(25/16 + 15/4) + 3/2*5/4 -q);

MH = [H11 H12; H21 H22];


    I11=((15/4)*a + 5*hi/2 + 3*hj/2) + b*(3*(25*9/16) +3/2*(15/4) - q);
```

```
MI = [I11];



     AA=eig(MA);
    eig1a(ii)=AA(1);

    BB=eig(MB);
    eig1b(ii)=BB(1);
    eig2b(ii)=BB(2);

     CC=eig(MC);
    eig1c(ii)=CC(1);
    eig2c(ii)=CC(2);
    eig3c(ii)=CC(3);

    DD=eig(MD);
    eig1d(ii)=DD(1);
    eig2d(ii)=DD(2);
    eig3d(ii)=DD(3);
    eig4d(ii)=DD(4);

    EE=eig(ME);
    eig1e(ii)=EE(1)
    eig2e(ii)=EE(2)
    eig3e(ii)=EE(3)
    eig4e(ii)=EE(4)
```

```
     FF=eig(MF);
    eig1f(ii)=FF(1);
    eig2f(ii)=FF(2);
    eig3f(ii)=FF(3);
    eig4f(ii)=FF(4);

     GG=eig(MG);
    eig1g(ii)=GG(1);
    eig2g(ii)=GG(2);
    eig3g(ii)=GG(3);

     HH=eig(MH);
    eig1h(ii)=HH(1);
    eig2h(ii)=HH(2);

     II=eig(MI);
    eig1i(ii)=II(1);

    ii=ii+1;
end

figure


plot(B,eig1a,'b',...
```

```
    B,eig1b,'b',B,eig2b,'r',...
    B,eig1c,'b',B,eig2c,'r',B,eig3c,'k',...
    B,eig1d,'b',B,eig2d,'r',B,eig3d,'k',B,eig4d,'g',...
    B,eig1e,'b',B,eig2e,'r',B,eig3e,'k',B,eig4e,'g',...
    B,eig1f,'b',B,eig2f,'r',B,eig3f,'k',B,eig4f,'g',...
    B,eig1g,'b',B,eig2g,'r',B,eig3g,'k',...
    B,eig1h,'b',B,eig2h,'r',...
    B,eig1i,'b')

%legend('1','2','3','4','5','6')
```

Bibliography

Abramowitz, M. & Stegun, I. 1972. *Handbook of Mathematical Functions.* New York: Dover.

Black, E. D. 2001, Am. J. Phys., 69, 79.

Bransden, B. & Joachain, C. 1983. *Physics of Atoms and Molecules.* Longman.

Burleigh Instruments Inc. 2002. *Operating Manual WA-1000 Wavemeter.* Burleigh Instruments Inc.

Coherent Inc. *Coherent Continuous Wave Tunable Lasers: 899 Series Laser Systems* (Training Course Lecture ed.). Coherent Inc.

Demtröder, W. 2003. *Laser Spectroscopy: basic concepts and instrumentation* (3rd Ed. ed.). Springer.

Duarte, F. & Hillman, L. (Eds.) 1990. *Dye Laser Principles With Applications.* Academic Press.

Griffiths, D. 1995. *Introduction to Quantum Mechanics.* Prentice Hall.

Hall, J. & Lee, S. 1976, Appl. Phys. Lett., 29, 367.

Hansch, T. & Couillaud, B. 1980, Opt. Commun., 35, 441.

Hecht, E. 2002. *Optics* (4th ed.). Addison-Wesley.

Itano, W. 2004, November. private communication.

Itano, W. & Wineland, D. 1981, Phys. Rev. A. *24*(3), 1364.

Jonsson, P., Parpia, F., & Fischer, C. 1996, Comp. Phys. Commun., 96, 301.

Kapitsa, P. 1951, Zh. Eskp. Teor. Fiz., 34, 242.

King, B. 1999. *Quantum State Engineering and Information Processing with Trapped Ions (Ph.D. thesis).* University of Colorado, Boulder.

King, E. 1982. *Operator's Manual CR-699 Ring Dye Laser.* Laser Innovations.

Kopfermann, H. 1958. *Nuclear Moments.* Academic Press Inc.

Leibfried, D. 2006. private communication.

Luc, P. & Gersrekorn, P. 1978. *Atlas du Spectre d'absorbtion de la molecule d'iode 14800-20000 cm-1.* Edition de Centre National de la Recherche Scientifique (CNRS).

Madsen, D. N., Balslev, S., Drewsen, M., Kjaergaard, N., Videsen, Z., & Thomsen, J. 2000, J. Phys. B: At. Mol. Opt. Phys., 33, 4981.

Metcalf, H. & van der Straten, P. 1999. *Laser Cooling and Trapping.* Springer.

Nagourney, W., Janik, G., & Dehmelt, H. 1983, Proc. Natl. Acad. Sci. USA, 80, 643.

Parpia, F., Fischer, C., & Grant, I. P. 1996, Comp. Phys. Commun., 94, 249.

Petrich, W. 1994. *Saturated Absorption Spectroscopy And Its Application to Laser Stabilization.*

Spectra Physics. *Wavetrain User's Manual Version 4.3.* Spectra Physics.

Wineland, D. & Itano, W. 1979, Phys. Rev. A *20*(4), 1521.

Woodgate, G. 1983. *Elementary Atomic Structure (Second Edition).* Oxford Science Publications.